An inter-comparison of the mass budget of the Arctic sea ice in CMIP6 models

Ann Keen[1], Ed Blockley[1], David Bailey[2], Jens Boldingh Debernard[3], Mitchell Bushuk[4], Steve Delhaye[5], David Docquier[6], Daniel Feltham[7], François Massonnet[5], Siobhan O'Farrell[8], Leandro Ponsoni[5], José M. Rodriguez[9], David Schroeder[7], Neil Swart[10], Takahiro Toyoda[11], Hiroyuki Tsujino[11], Martin Vancoppenolle[12], and Klaus Wyser[6]

1: Met Office Hadley Centre, Exeter, UK.
2: National Center for Atmospheric Research (NCAR), Boulder, CO, USA.
3: Norwegian Meteorological Institute, Oslo, Norway.
4: Geophysical Fluid Dynamics Laboratory (GFDL), Princeton, NJ, USA.
5: Georges Lemaître Centre for Earth and Climate Research (TECLIM), Earth and Life Institute, Université catholique de Louvain, Louvain-la-Neuve, Belgium.
6: Rossby Centre, Swedish Meteorological and Hydrological Institute (SMHI), Norrköping, Sweden.
7: Centre for Polar Observations and Modelling (CPOM), University of Reading, Reading, UK.
8: CSIRO Oceans and Atmosphere, Aspendale, Victoria, Australia.
9: Agencia Estatal de Meteorología (AEMET), Madrid, Spain.
10: Environment and Climate Change Canada (ECCC), Canadian Centre for Climate Modelling and Analysis, Victoria, BC.
11: Meteorological Research Institute, Japan Meteorological Agency, Tsukuba, Japan.
12: Laboratoire d'Océanographie et du Climat et Institut Pierre-Simon Laplace (LOCEAN-IPSL), Paris, France.

Correspondence to: Ann Keen (ann.keen@metoffice.gov.uk)

Abstract. We compare the mass budget of the Arctic sea ice for 14 models submitted to the latest Climate Model Inter-comparison Project (CMIP6), using new diagnostics that have not been available for previous model inter-comparisons. Using these diagnostics allows us to look beyond the standard metrics of ice cover and thickness, to compare the processes of sea ice growth and loss in climate models in a more detailed way than has previously been possible.

For the 1960-89 multi-model mean, the dominant processes causing annual ice growth are basal growth and frazil ice formation, which both occur during the winter. The main processes by which ice is lost are basal melting, top melting and advection of ice out of the Arctic. The first two processes occur in summer, while the latter process is present all year. The sea-ice budgets for individual models are strikingly similar overall in terms of the major processes causing ice growth and loss, and in terms of the time of year during which each process is important.

However, there are also some key differences between the models. The relative amounts of frazil and basal ice formation varies between the models. This is, to some extent at least, attributable to exactly how the frazil growth is formulated within each model. There are also differences in the relative amounts of top and basal melting.

As the ice cover and mass decline during the 21st century, we see a shift in the timing of the top and basal melting in the multi-model mean, with more melt occurring earlier in the year, and less melt later in the summer. The amount of basal growth in the autumn reduces, but the amount of basal growth later in the winter increases due to the ice being thinner. Overall, extra ice loss in May-June and reduced ice growth in October-November is partially offset by reduced ice melt in August and increased ice growth in January-February. For the individual models, changes in the budget components vary considerably in terms of magnitude and timing of change. However, when the evolving budget terms are considered as a function of the changing ice state itself, behaviours common to all

45 the models emerge, suggesting that the sea ice components of the models are fundamentally responding in a broadly consistent way to the warming climate.

Additional results from a forced ocean-ice model show that although atmospheric forcing is crucial for the sea ice mass budget, the sea ice physics also plays an important role.

50 **1. Introduction**

Sea ice is a key component of the climate system, and the observed decline in Arctic ice cover provides a very visible indicator of climate change. Between 1979 and 2018, Arctic September sea ice extent has declined at a rate of nearly 13% per decade (IPCC, 2019). The ice has also thinned, and there has been a transition to a greater

55 coverage of younger ice: the proportion of Arctic ice cover that is more than 5 years old decreased by 90% between 1979 and 2018 (Kwok, 2018; Stroeve and Notz, 2018; IPCC, 2019). The ice also moves more quickly (Olanson and Notz, 2014).

Global coupled climate models are the most comprehensive tools that we have for predicting how the Arctic ice will change in the future, as they can represent a range of processes that control the seasonal cycle of ice growth

60 and melt, and so have the potential to represent the changing nature of the ice itself. However, model projections show a wide spread in the rate of ice decline, both during the period for which we have observations, and also into the future as we move towards a seasonally ice-free Arctic (Massonnet et al. 2012; Notz and Stroeve, 2016; SIMIP community, 2020).

Some of this spread is an inevitable consequence of the internal variability of the climate system, and the

65 uncertainly in future forcing. For example, Jahn et al. (2016) find that internal variability causes an uncertainty of 21 years in predicting the year in which the Arctic first becomes seasonally ice-free using a large (40 member) ensemble of model runs, with an additional uncertainty of 5 years due to scenario uncertainty. However, some spread is likely to be due to differences between the model's representation of the sea ice and other components of the climate system. Spread may also arise from differences in initial conditions (Hawkins and Sutton, 2009;

70 Melia et al., 2015).

For previous model inter-comparisons (CMIP3 and CMIP5), primarily only changes in ice extent, volume (or mass), and ice motion (Tandon et al. 2018, Rampal et al., 2011) have been considered, as these quantities are readily available as model output that can be compared directly to one another, and to observational or reanalysis references. However, there is an increasing appreciation that in order to understand the reasons for differences in

75 projections of ice state, we need to be able to look 'behind the scenes' to understand the balance of different processes that drive the evolving ice state, and how these change as the ice declines.

For the CMIP3 models, Holland et al. (2010) calculated the changes in ice mass due to melt, growth and divergence using monthly mean model values of ice thickness and velocity. They found an appreciable variation in the size and relative importance of changes in these budget components between the models as the sea ice

80 declines. For individual models, diagnostics may be available that allow a more comprehensive decomposition of the model budget. For example, Keen and Blockley (2018) studied changes in the volume budget of the Arctic sea ice in a CMIP5 model under a range of forcing scenarios, considering both annual and seasonal changes in the individual processes causing ice growth and loss.

For the latest generation of sea ice models (the CMIP6 models), a Sea-Ice Model Intercomparison Project (SIMIP)

85 has been established, which has defined a comprehensive set of diagnostics allowing the intercomparison of the

mass, energy and freshwater budgets of the sea ice (Notz et al., 2016). In this study we use these new diagnostics to present a first intercomparison of the mass budget of the sea ice for 14 of the CMIP6 models. Note that this is a subset of the CMIP6 models, just including those for which the required outputs were available. We first look at the mean mass budget for a reference period, to determine the similarities and differences between the model

90   budgets during a period with relatively little change in the ice state. We then consider how the budgets change as the ice declines during the 21st century, and how changes in the budget components relate to changes in the ice state and the global temperature.

In Sect. 2 we describe the models and forcing scenarios used, and in Sect. 3 we intercompare the modelled ice area and mass. In Sect. 4 we consider the mean mass budget during a reference period, and in Sect. 5 we investigate

95   how the budget evolves during the 21st century. In Sect. 6 we summarise and discuss our results.

2. Models and methodology

In this study we analyse data from 14 CMIP6 models, originating from 8 different modelling centres. We also

100   analyse data from 3 configurations of the NEMOCICE ocean-sea ice model forced by atmospheric reanalysis, which has a similar formulation to one of the CMIP6 models used in this study (HadGEM3-GC3.1-LL). These models, and the data provided from each, are listed in Table 1. Key details about the formulation of each model are summarised in Table 2, with a brief description of each in Appendix A. For each model, the ice area and mass, and the area weighted monthly-mean ice mass budget terms were calculated over the domain shown in Fig. 1,

105   covering the Arctic Ocean Basin (Central Arctic plus the Beaufort, Chukchi, East Siberian, Laptev, Kara Seas) and the Barents Sea. Unless otherwise stated, all results shown in the paper are integrals over this analysis region and so do not represent the entire Northern Hemisphere ice-covered region, especially in winter. Multi-model means are calculated by first averaging all the realizations for each individual model (where appropriate), and then averaging the resulting ensemble-means. The mass budget terms are defined in Appendix E of Notz et al.

110   (2016), and summarised here for completeness:

- Basal growth: ice growth at the base of existing ice.
- Frazil ice formation: ice formation in supercooled open water.
- Top melt: melting at the top surface of the ice.
- Basal melt: melting at the base of the ice.

115   - Lateral melt: melting at the sides of the ice.
- Snowice: ice formation due to the transformation of snow to sea ice.
- Evapsubl: the change in ice mass due to evaporation and sublimation.
- Advection: the change in ice mass due to ice being advected into or out of the analysis domain.

120   The monthly mean data was calculated for the period 1960-2100 from model integrations using the CMIP6 Hist forcing scenario for the period 1960-2014, and SSP5-8.5 thereafter (Gidden et al, 2019). The SSP5-8.5 scenario was primarily chosen because for the majority of participating modelling centres this was the first scenario to be run, but it also has the advantage of being the scenario with the highest warming signal, so that we see relatively large changes in the ice state and the budget terms during the 21st century.

125

In order to better understand the relative roles of atmospheric forcing and sea ice model physics, results from three forced ocean-ice simulations are also included. All of them use the same ocean and sea ice models as the UK CMIP models (HadGEM3-GC31-LL, HadGEM3-GC31-MM and UKESM1-0-LL), with changes to both the parameter settings and the atmospheric forcing datasets. Further details of the settings and forcings used can be found in Table 3.

We also compare the modelled ice state with a number of observational and reanalysis datasets. We calculate the ice area over our analysis domain (Fig. 1) using monthly mean values from 3 observational products:

- The second version of the global sea-ice concentration climate data record (OSI-450) from the European Organisation for the Exploitation of Meteorological Satellites (EUMETSAT) Ocean Sea Ice Satellite Application Facility (http://osisaf.met.no/p/ice/ice_conc_cdr_v2.html, OSI-SAF, 2017; Lavergne et al., 2019).
- The first and second versions of the Met Office Hadley Centre's sea ice and sea surface temperature data set: HadISST1.2 (https://www.metoffice.gov.uk/hadobs/hadisst/, Rayner et al., 2003) and HadISST.2.2 (https://www.metoffice.gov.uk/hadobs/hadisst2/, Titchner and Rayner, 2014).

For ice mass we use monthly mean sea-ice thickness from the Pan-Arctic Ice-Ocean Modeling and Assimilation System (PIOMAS) (http://psc.apl.uw.edu/research/projects/arctic-sea-ice-volume-anomaly/data/, Zang and Rothrock, 2003) to calculate the ice volume, which is then converted to mass using the constant value of 917 kg m^{-3} for the ice density used in PIOMAS. While this is not an observational dataset, it provides a useful reference as it has been well studied and validated against observations (for example Stroeve et al., 2014, Wang et al., 2016).

3. Model inter-comparison of mean sea ice state

We first compare the ice area and mass simulated by the different models. We consider the seasonal cycle for the period 1990-2009, in order to compare model results to present-day observations and the PIOMAS reanalysis. We also consider the evolution of the ice area and mass from 1960 to 2100, so that we can put the budget changes into context. Note that the values of ice area and mass shown here, both for the models and observational datasets, are values for the Arctic domain shown in Fig. 1, and do not represent the whole ice-covered region.

3.1 1990-2009 seasonal cycle

During the period 1990-2009, there is a spread of 0.7 million km^2 in the March ice area simulated by the models (Fig. 2a). Despite the winter ice cover being bounded to some extent by the analysis region, the modelled values range from 8.4 to 9.1 million km^2, compared with a range of 8.2 to 8.7 million km^2 for the three observational datasets. The observational range as quoted here is the spread in the +/- 1 standard deviation limits for the three datasets. In September we see a much larger spread in modelled ice area (3.4 million km^2), although most models fall within +/- 1 standard deviation of at least one of the datasets, which show a greater interannual variability for September than for March. One model in particular (NCAR_CESM2_CAM) has an especially large seasonal cycle and low ice area in September, possibly because of its relatively low ice mass (Fig 2b and discussed below). The magnitude of the modelled seasonal cycle in ice area varies between 3.2 and 6.0 million km^2. The observational datasets have their minimum ice area in September, and while 4 of the models clearly capture this, the remainder have their seasonal minimum in August or have August and September values that are very similar.

The models that have a minimum sea ice area in August all include the NEMO ocean model, and later we will see that the forced ocean-ice simulations (which use NEMO) also have their minimum sea ice area in August.

170   There is a large spread in modelled values of the ice mass, with the differences between models being much larger than the variability suggested by the PIOMAS reanalysis for all months (Fig. 2b). For example, in March the PIOMAS range (+/- 1 standard deviation) is 16×10^3 to 20×10^3 Gt, while the CMIP6 model values range from 13×10^3 to 29×10^3 Gt. While there are some differences in the magnitude of the seasonal cycles of ice mass, this is not as pronounced as it is for the ice area as the model spread in ice mass is relatively consistent all year. The

175   magnitude of the seasonal cycle ranges from 8.1×10^3 to 12.1×10^3 Gt, compared to the value of 10.1×10^3 Gt for the PIOMAS reanalysis. All models have their seasonal maximum ice mass in May, and minimum in September, consistent with the PIOMAS reanalysis. The models with the largest ice mass tend to be those with the smallest seasonal cycle in sea ice area, and vice versa. This is probably because a model with a smaller mass of sea ice is likely to have relatively thin ice, and so more ice cover would be lost for a given reduction in ice mass.

180

3.2 Evolution from 1960 to 2100

The models show a wide range of rates of decline in both March and September ice area (Fig. 3a). For example, the date at which the September ice area first falls below 1 million km^2 varies from 2019 to 2062 overall, although

185   it is between 2025 and 2040 for the majority of models. By the end of the 21st century, all the models have completely lost their September ice cover. The evolution in March ice area starts to show a divergence between the models from about 2040, increasing significantly from about 2070. Many models show a steepening in the rate of decline of March ice area later in the 21st century, after their summer ice cover has melted out. Bathiany et al. (2016) found a similar steepening in the rate of winter decline for CMIP5 models. By the end of the 21st century

190   there is a large spread in modelled March ice area: the fraction of ice area lost relative to 1960-89 ranges from 8% to 90%.

There are large differences between the models in terms of the evolution of their ice mass (Fig. 3b). Between 1960 and 2030, some models show an ongoing decline in ice mass, others have a period where the ice mass remains relatively stable before it starts to decline, and a few models show an increase in ice mass before the decline. By

195   the 2030s the models have a much lower spread in values of ice mass, with a range of 8.7×10^3 Gt, compared to 16.4×10^3 Gt during the reference period 1960-89. By this stage there is very little mass of summer ice remaining, and so the winter ice mass is limited to the amount that can grow during a single season. Some models show a distinctive slowing in the rate of decline of ice mass later in the 21st century, whereas other models show a more uniform rate of decline.

200

3.3 Ice state in global context

To help put the ice state and its evolution in a wider context, we consider the evolution of global-mean near-surface temperature for the models (Fig. 4a). By the end of the 21st century, the warming relative to the 1960-89

205   mean ranges from 3.9 to 7.2 degrees. Models with a larger decrease in March ice area by the end of the 21st century tend to be those with the larger temperature increase. Previous studies have found a linear relationship between sea ice area and global-mean temperature for example Winton (2011), Mahlstein and Knutti (2012), Stroeve and Notz (2015), and Rosenblum and Eisenman (2017), and this is also the case for the CMIP6 models considered here (Fig. 4b).

210

4. Mean sea ice mass budget for 1960-1989

We now consider the mass budget of the Arctic sea ice, as defined in Sect. 2 and also in Notz et al. (2016). We
215 start by looking at the model data for a reference period 1960-89, chosen as a time when the ice cover and mass
is relatively stable. We first consider the multi-model mean budget, and then look at the differences between
models.

4.1 Multi-model mean
220

Figure 5a shows the budget terms for the mass budget of the Arctic sea ice, averaged over the analysis region
shown in Fig. 1, for the multi-model mean for the reference period 1960-89. The black line shows the total amount
of ice growth or loss each month, with net ice loss occurring from May to September, and net ice growth from
October to April. Most of the increase in ice mass results from growth at the base of existing ice, which occurs
225 between September and May and represents 81% of the total annual ice growth (Fig. 5b). Frazil ice formation in
open water accounts for 18%, with the small remainder due to snow-ice formation. Most of the ice loss occurs
during the summer, with 51% of the annual mean ice loss caused by basal melting due to heat from the ocean, and
24% by melt at the ice surface (Fig. 5b). The monthly maximum ice melt occurs in July, with both top and basal
melt peaking at this time, and the basal melt continues further into the late summer that the top melt (Fig. 5a). Ice
230 lost by advection out of the region accounts for 20% of the total (Fig. 5b), and this is likely to be dominated by
loss through the Fram Strait. The advective ice loss occurs all year, and although it is greater during the winter
than the summer, the magnitude of the seasonal cycle is far smaller than that for either the top or basal melting
(Fig. 5a).

235 In summary, for the 1960-89 multi-model mean the dominant process causing ice growth is basal ice growth,
followed by frazil ice formation, and the dominant processes causing ice loss are basal melting, top melting and
advection out of our analysis region.

4.2 Inter-comparison of the CMIP6 models
240

Figures 6 and 7 show the annual means and seasonal cycles of the budget terms for each individual model. Note
that some models do not generate all the terms, and some models have terms missing (see Table 1). It is striking
to see how similar the model budgets are, at least in a broad sense. For example, in all the models we see:
- more basal ice growth than frazil ice formation (although the amounts are nearly even for MRI-ESM2)
245   (Fig. 6),
- virtually no ice growth between June and August (Fig. 7),
- more basal melting than top melting (although the difference is small for the UK models and
  CSIRO_ACCESS-CM2) (Fig .6),
- a maximum in ice melting in July, with a peak in both top melting and basal melting (Fig. 7),
250 - basal melt continuing later into the autumn than top melting (Fig. 7),
- and a relatively symmetric seasonal cycle centred around the maximum net ice loss in July.

However, there are also some notable differences between the model budgets, which we describe below.

Ice growth

255 The ratio between basal ice growth and frazil ice formation varies significantly between the models. For example, for both the GFDL models almost all the annual ice growth is due to basal ice growth, whereas for the MRI-ESM2.0 model 53% of the annual growth is due to basal growth, and 46% to frazil ice formation. This different partitioning appears to relate to specific settings within the sea ice model, in particular the minimum thickness of frazil ice that is allowed to form. In the GFDL models there is no minimum thickness imposed, and so the models

260 can grow arbitrarily thin frazil ice. Hence the frazil ice may transition to congelation growth more quickly than in other models. MRI-ESM2.0 has a minimum frazil thickness of 20cm, which is the highest value of the models considered here. Additionally, this model has a maximum ice cover set (0.98), so there is always some open water where frazil ice can form. In general, the models with a larger minimum frazil thickness tend to have a higher proportion of frazil ice formation.

265 If we consider the total amount of winter ice growth (here taken as the sum of the frazil and basal growth terms), the spread in modelled values is 3.8×10^3 Gt, compared to the larger range of 5.8×10^3 Gt for the basal growth alone. The month in which the amount of frazil ice formation peaks varies from October (UK models and CSIRO_ACCESS-CM2) through November (EC-Earth3 and EC-Earth3-Veg) to December for the remaining models. The amount of basal growth peaks in December for most of the models.

270

Ice melt

The relative amount of basal and top melting also varies considerably between the models, with top melting ranging from 28% to 91% of the amount of basal melt (Fig. 6). The UK models (HadGEM3-GC31-LL, HadGEM3-GC31-MM and UKESM1-0-LL) together with CSIRO-ACCESS-CM2 have almost as much ice lost

275 by top melting as by basal melt, in contrast to the other models which have considerably more basal melt than top melt (Fig. 6). The UK and CSIRO models have common atmosphere and sea ice components. The models agree very well on the amount of top melting late in the season (Aug-Sep). However, the onset of melt (May-June), and peak in melting in July shows much more variability (Fig. 7). This is consistent with the former being mainly related to the solar zenith angle, whereas the latter is also related to other factors like ice/snow surface temperature

280 and surface albedo. Six out of the 14 models have more top melting than basal melting in July (Fig. 7), and these are the models with most top melting overall (Fig. 6). Some models have a fairly symmetrical peak in basal melting (for example the UCLouvain models and also the NCC_NorESM2-LM model.), whereas some have a more pronounced 'tail' of melt further into autumn (for example MRI_ESM2.0, GFDL).

285 ### Ice advection

All the models show a net advection of ice out of the analysis region (Fig. 6). This is likely to be dominated by export through the Fram Strait. The net ice loss by advection varies from 1.8×10^3 to 3.7×10^3 Gt per year between the models and comprises between 15% and 30% of the total annual ice loss. There is no strong agreement between models as to how this export varies during the year. One model (CSIRO_ACCESS-CM2) has a distinctive

290 seasonal cycle with most of the ice export occurring between October and April, and net ice *import* during July. Several of the remaining models have a minimum net export of ice in August, but overall there is considerable variability between the models in terms of the amount and timing of the annual ice export.

5. Projections of the sea ice mass budget during the 21st century

We now consider how the mass budget of the CMIP6 models changes during the 21st century as the ice cover and mass declines, and the environment warms. Figure 8 shows the evolution of the annual mean budget terms for each model. Again, it is reassuring to see many similarities in the behaviour of the different models. For all models the magnitude of each component tends to decrease with time, consistent with the reducing mass of the ice. Models with larger changes in the budget components tend to be those with larger reductions in the ice mass. The amount of ice lost by advection tends to decrease relatively quickly compared to the decline in ice growth and melt, and models with a more rapid decline in basal ice growth tend to also have a more rapid decline in top and basal melt. Broadly speaking, for each model the relative amount of basal and top melting tends to persist: for example, models with considerably more basal melt than top melt during the reference period still show this towards the end of the 21st century. Some of the budget components initially increase in magnitude, before declining later in the integration. We will now consider each of the larger budget components in turn, and in particular how the ice state itself impacts the evolution of each budget term

Basal ice growth

Overall, all the models show a gradual decrease in the total amount of basal ice growth as the climate warms (Fig. 8). For a few models, for example UKESM1-LL, there is initially a slight increase in basal ice growth before the decline. As the climate warms, all the models initially show an increasing amount of basal ice growth *per unit area of ice*, consistent with the ability of thinner ice to grow more quickly than thicker ice (Fig. 9a). Later, as the warming continues, the basal growth per unit area of ice decreases as the rising temperatures act to suppress the ice growth (Fig. 9a). The evolution of the *total* amount of basal growth seen in Fig. 8 arises from a combination of the 'in situ' changes of Fig. 9a, modified by the fact that the area of sea ice over which basal growth can occur is itself decreasing. Models with the largest decline in basal ice growth by the end of the 21st century tend to be those with the larger decline in winter ice cover, and Figures 11a and 11b show that there is a robust relationship common to all the models between the change in the mass of basal growth and both the ice area and ice mass.

Frazil ice formation

As the climate warms, many models initially show a small increase in the total amount of frazil ice formation relative to the 1960-89 reference period (Fig. 10a). This is probably because as the ice area declines there is a greater area of open water in which frazil ice can form. Eventually the amount of frazil ice formation reaches a maximum, then starts to decline until by 2090s all the models have less frazil ice formation than they did during 1960-89. This is consistent with the ocean warming so that an increasing area of the ocean either no longer falls below the freezing temperature or does so for a shorter period of the year. The timing of the changes in frazil ice formation varies considerably between the models. For example, the decade in which the amount of frazil ice formation becomes consistently less than the reference value varies from the 2030s to the 2080s.

Top melting

All the models show an initial increase in the total amount of ice melted at the top surface relative to 1960-89, which continues until at least the 2030s for the majority of models. (Fig. 10b). As the warming continues, this reverses as the surface area of the ice reduces, so that the total amount of top melt declines. Towards the end of

the 21ˢᵗ century, all models have less annual total top melt than they did during the 1960-89 reference period. The timing of the maximum amount of top melt varies between the models (Fig. 10b) and is related to the rate of decline of the ice area (Fig. 11c). The amount of top melt *per unit area of the ice* increases for all the models (Fig. 9b) and continues to increase later into the 21ˢᵗ century than the total melt term does. (Figs. 9b and 10b). Towards

340   the end of the 21ˢᵗ century, the top melt per unit area starts to decrease (Fig. 9b), presumably because the ice cover that remains is restricted to relatively high latitudes, and so receives less solar radiation. Again the exact timing of this varies between the models.

Basal melting

345   For many of the models, the total amount of basal melting each year starts to increase as the climate warms (Fig. 10c), then decreases later in the integration as the ice cover shrinks. The GFDL models and the MRI model initially show little change in the total basal melt, which then decreases later in the integration. By the end of the 21ˢᵗ century all the models lose less ice each year by basal melting than they did during the reference period. The time at which the total amount of basal melt starts to decrease is related to the ice area (Fig. 11d), with a maximum

350   about of basal melt occurring for an annual mean ice cover of approximately 6 million. Per unit surface area of the ice, all the models show an ongoing increase in basal melt throughout the 21ˢᵗ century as the ocean warms (Fig. 9c), with a greater increase seen in the models with larger reductions in winter ice cover.

Ice advection

355   For all the models, the amount of ice lost by advection declines relatively quickly compared to the other terms (Fig. 8). By the 2040s the majority of models lose less than 1.0×10^3 Gt of ice each year by advection. The amount of advective ice loss is strongly related to the change in ice mass (Fig. 11e).

Thus far we have only considered how the annual mean budget components evolve, but of course there are changes

360   to the seasonal cycle of the budget components as well. Figure 12 shows how the seasonal cycle of the multi-model mean budget has changed by the 2040s. The timing of the top and basal melting has shifted, with more melt occurring earlier in the year (especially during June), and less later in the summer (especially during August). The amount of basal growth in the autumn reduces, but there is increased basal growth later in the winter associated with the thinner ice in this time period. Overall, extra ice loss in May-June and reduced growth in

365   October-November is partially offset by reduced ice melt in August and increased ice growth in January-February.

In summary, there are a number of factors affecting how each budget component changes as the climate warms, including the changing atmospheric and oceanic forcing, and also the ice state itself, especially the ice area. For some of the budget components, initial increases due to changes in forcing are later offset by the declining ice

370   area.

6. Discussion and conclusions

375   We have compared the mass budget of the Arctic sea ice for 14 CMIP6 models, using new diagnostics not available for previous model inter-comparison studies (Notz et al., 2016). In common with CMIP3 and CMIP5

models, the CMIP6 models we have analysed here show a large spread in their ice area and mass, both during a 'present day' evaluation period, and also as the ice declines during the 21st century (SIMIP community, 2020).

380   One of the most striking results of this study is the broad agreement between the mean mass budget of the individual models, both in terms of the dominant processes, and also the time of year when each process is important. For the multi-model mean, the dominant processes causing annual ice growth are basal ice growth (~80%) and frazil ice formation (~20%), which both occur during the winter. The dominant processes by which ice is lost are basal melting (~50%), surface melting (~25%) and advection of ice out of the Arctic (~20%). The

385   two first processes occur in summer, while the latter process is present all year long.

For the individual models, the relative amount of frazil and basal growth varies considerably. The ratio between the two is related to the details of how the frazil ice formation is defined within each model, and in particular to the minimum thickness of frazil ice. Models that can form thicker frazil ice tend to have a greater proportion of

390   their ice growth defined as frazil ice. When the frazil and basal ice growth terms are combined, there is less spread between the models. The relative amounts of top and basal melt also vary between the models. A number of factors are likely to contribute to this, including the melt pond formulation, the radiation scheme and the atmospheric forcing. It has not proved possible in this study to identify a common factor to explain the differences in the ratio of top and bottom melting.

395

The mean mass budget is influenced by both the sea ice physics, and also the atmosphere and ocean forcing. By comparing CMIP6 models we are effectively varying all these factors at once, so we also include here some budget data for three integrations using a forced ocean-ice model with the same sea ice and ocean components as the HadGEM3-GC31-LL model. Using this forced model, we can look at the impact of changing sea ice physics or

400   atmospheric forcing alone (Table 3). It is noteworthy that the default forced simulation differs strongly from the HadGEM3-GC31-LL simulation despite the same sea ice settings (Fig. 13). In contrast to HadGEM3-GC31-LL, sea ice mass and area are smaller in the forced simulation than in PIOMAS, and HadISST and OSI-SAF respectively. The stronger bottom and surface melt in the forced simulation (Fig. 14 a and b) leads to a stronger annual cycle and smaller sea ice area during summer (Fig. 13a). This suggests that the interaction with the

405   atmosphere is responsible for the overestimation of sea ice mass in HadGEM3-GC31-LL. Applying sea ice physics which results in improved sea ice evolution in a stand-alone sea ice simulation (Schroeder et al., 2019), reduces the basal melt (Fig. 14c) and slightly increases the late winter basal growth (not shown), which in turn increases sea ice area and mass (Fig. 13). Applying DFS atmospheric forcing instead of CORE forcing increases the top melt and decreases the basal melt, resulting in higher sea ice area and mass. These comparisons

410   demonstrate that both model sea-ice physics and atmospheric forcing are important in driving the differences among models in the sea ice mass budget.

We have also looked at how the mass budget changes as the climate warms during the 21st Century. For the multi-model mean, the timing of the top and basal melting shifts, with more melt occurring earlier in the year (especially

415   during June), and less melt later in the summer (especially during August). The amount of basal growth in the autumn reduces, but there is increased basal growth later in the winter associated with the thinner ice in the future

projections compared to the present. Overall, extra ice loss in May-June and reduced growth in October-November is partially offset by reduced ice melt in August and increased ice growth in January-February.

420   Comparing the responses of the individual models, the timing and magnitude of change in the mass budget components varies considerably. We have seen that there are a number of factors affecting how each budget component changes as the climate warms, including the changing atmospheric and oceanic forcing, and also the ice state itself, especially the ice area. However, when considered as a function of the changing ice state itself, common behaviours emerge, which suggests that the mass budgets of the models are fundamentally responding

425   in a broadly consistent way to the warming climate.

The fact that the sea ice budgets are similar in these CMIP6 models, but sea ice area and volume are not, makes a case that the current biggest issue for climate change studies is not the sea ice physics but the atmospheric forcing. On the other hand, it is not necessarily the case that the degree of similarity in the mass budget of these CMIP6

430   models is a good thing. From table 2 we see that sea ice model diversity is quite poor in these models, and it could be argued that we are not sampling enough uncertainly in sea ice physics. For example, none of these models use the most recent rheology or thermodynamic developments. Ideally, we would be able to compare both the modelled ice state and the budget components against observational datasets, to assess whether models are able to generate the correct ice state for the correct reasons. While some validation of the underlying processes that

435   determine the ice area is possible (for example Holmes et al, 2019), this remains more difficult for the mass budget terms.

In summary, new diagnostics available for CMIP6 models have allowed a more detailed inter-model comparison of the Arctic sea ice mass budget than has previously been possible. This study has provided a first comparison

440   of these diagnostics for a subset of the CMIP6 models by comparing budget terms integrated over the Arctic Ocean. As more CMIP6 model data becomes available, it would be good to examine the budget of a wider range of models. Further work could also include a comparison of the mass budget of snow on sea ice, an investigation into the spatial distribution of the ice and snow budget terms, and a linking of the budget changes to changes in the wider climate, both in the Arctic and beyond.

445

Appendix A: Model descriptions

Here we provide a brief summary for the CMIP6 models used in this study. Further details can be found in the

450   cited references.

AEMET_EC-Earth3 and SMHI_EC-Earth3-Veg

EC-Earth is an Earth System Model that comprises coupled component models for atmosphere, ocean, sea ice and land (Hazeleger et al., 2012). Both versions used in this study, namely EC-Earth3 and EC-Earth3-Veg, have the

455   same model configuration for atmosphere, ocean and sea ice. Besides, EC-Earth3-Veg has also an interactive vegetation module. The atmosphere component is represented by the Integrated Forecasting System (IFS), cycle 36r4, of the European Centre for Medium-Range Weather Forecasts (ECMWF). The atmospheric grid is T255L91 with a nominal horizontal resolution of about 100km. IFS contains 91 vertical levels in hybrid coordinates, in

which its highest vertical level reaches up to 0.01 hPa and, therefore, is a stratosphere resolving atmospheric
460   model.

The EC-Earth's ocean component is represented by the version 3.6 of NEMO (Madec, 2016) using the
ORCA1L75 grid defined by a tripolar grid with poles placed at Northern America, Siberia, and Antarctica. It has
a horizontal resolution of about 1 degree and 75 vertical levels, 8 of them being placed in the first 10 m of the
water column. The ocean component includes the version 3 of the Louvain-la-Neuve sea ice model (LIM3;
465   Rousset et al., 2015). LIM3 is a dynamic-thermodynamic model that accounts for a prognostic sea ice thickness
scheme (Thorndike et al., 1975; Lipscomb, 2001) defined by 5 thickness categories. LIM3 applies the elastic-
viscous-plastic (EVP) rheology for ice dynamics and also uses the ORCA1L75 grid. The sea ice model
thermodynamics is characterized by an energy-conserving halo-thermodynamic scheme (Bitz and Lipscomb,
1999) with 2 ice layers and 1 snow layer, for which the snow conductivity term is set to 0.27 W m-1 K-1. The
470   surface albedo depends on the ice surface temperature, ice thickness, snow depth, and cloudiness. The radiation
absorbed by the ice follows Beer's law and does not infiltrate into the snow. LIM3 does not account for the lateral
melting. Melt-ponds are not included in the sea ice model. The coupling between the atmosphere and ocean-sea
ice components is performed using the OASIS3 coupler.

For both EC-Earth3 and EC-Earth3-Veg, the H-TESSEL scheme, cycle 36r4 (same as IFS), is used for the land
475   surface (van den Hurk et al., 2000). H-TESSEL is also based on the T255L91 grid and has 8 horizontal tiles used
in the land surface/exchange scheme. In addition, EC-Earth3-Veg comprises the version 4 of the Lund-Potsdam-
Jena General Ecosystem Simulator (LPJ-GUESS) dynamic vegetation model (Smith et al., 2014). As the
atmospheric and ocean-ice components, H-TESSEL has a 45-minute time step, while LPJ-GUESS has a 1-day
time step.

480

CanESM5

The CanESM5 model (Swart et al., 2019) uses the CLASS-CTEM3.6 land surface model and the CanAM5
atmospheric model at T63 spectral resolution (approx. 2.8 degrees) and with 49 vertical levels. These are coupled
to the NEMO 3.4.1 model, with 45 vertical levels, and the LIM2 sea ice model (Madec, 2016; Fichefet and
485   Morales Maqueda, 1997) at 1 degree horizontal resolution.

The sea ice model component uses the elastic-viscous-plastic (EVP) rheology and melt-ponds are parameterised
as a function of surface temperature with a fraction ranging between 0 and 25% of the ice cover.

490   CESM2-CAM and CESM2-WACCM

The CESM2 models are built from the CESM2.1 configuration described in Danabasoglu et al. (2019). It uses the
CAM6 atmosphere model and the CLM5 land surface model at nominal 0.9 x 1.25 degree resolution, coupled to
the POP 2.0.1 ocean and the Los Alamos sea ice model (CICE) at nominal 1 degree (gx1) resolution.

The sea ice model component is based upon version 5.1.2 of the CICE sea ice model of Hunke et al. (2015). The
495   CICE model uses a prognostic ice thickness distribution (ITD) with five thickness categories. The standard CICE
elastic–viscous–plastic (EVP) rheology is used for ice dynamics. The model uses mushy-layer thermodynamics
and prognostic sea ice salinity (Turner et al., 2013) configured with 8 layers of ice and 3 of snow.

Radiation is calculated using the delta-Eddington scheme of Briegleb and Light (2007), with melt-ponds modelled on level, undeformed ice, as in Hunke et al. (2013).

500

CSIRO_ARCCSS_ACCESS-CM2

The CSIRO_ARCCSS_ACCESS-CM2 uses atmosphere and sea mode components derived from the HadGEM3-GC3.1 models – including the MetUM atmosphere, using the Global Atmosphere 7.1 (GA7.1) configuration of Walters et al. (2017), and the Global Sea Ice 8.1 (GSI8.1) configuration of the CICE sea ice model described in

505 Ridley et al. (2017). These are combined with version 2.5 of the CABLE land surface model and version 5.1 of the MOM ocean model.

As for the HadGEM3-GC3.1 models, the sea ice model component is based upon version 5.1.2 of the CICE sea ice model (Hunke et al., 2015), using five thickness categories and the standard elastic–viscous–plastic (EVP) rheology. The model uses the Bitz and Lipscomb (1999) multi-layer vertical thermodynamics with 4 layers of ice

510 and 1 of snow. Atmosphere-ice coupling is performed separately for each ice thickness category using the method of West et al., (2016).

Radiation is calculated using CICE's "default" CCSM3 scheme (see Hunke et al., 2015) which uses separate albedos for visible (< 700 nm) and near-infrared (> 700 nm) wavelengths for both bare ice and snow. The scheme has been ported into JULES where the surface exchanges are calculated. Prognostic melt ponds are included using

515 the CICE topographic melt pond formulation of Flocco et al. (2010). Melt pond evolution is calculated in CICE with pond fraction and depth being passed through the coupler for use within the surface exchange scheme (albedo).

GFDL-CM4 and GFDL-ESM4

520 The GFDL-CM4 and GFDL-ESM4 models use the AM4.0 atmosphere/land model as documented in Zhao et al. (2018) with 100km horizontal resolution. CM4 has 33 vertical atmospheric levels whereas ESM4 has 49 vertical levels. These are coupled to the ocean and sea ice models MOM6 and SIS2, which are run under the OM4.0 configurations described in Adcroft et al. (2019). CM4 and ESM4 use nominal 0.25 and 0.5 degree horizontal ocean and sea ice resolutions, respectively. Both models have 75 vertical ocean layers. The CM4 model is

525 documented in Held et al. (2019).

The SIS2.0 sea ice component used in both GFDL-CM4 and GFDL-ESM4 models is documented in Adcroft et al. (2019).

HadGEM3-GC31-LL and HadGEM3-GC31-MM

530 The HadGEM3-GC31 models use the Global Coupled configuration 3.1 (GC3.1) of the HadGEM3 model introduced by Williams et al. (2017). This model comprises the MetUM atmosphere and JULES land models using the Global Atmosphere 7.1 (GA7.1) and Global Land 7.0 (GL7.0) configurations documented by Walters et al. (2017). These are coupled to the NEMO ocean and CICE sea ice models using the Global Ocean 6.0 (GO6.0) and Global Sea Ice 8.1 (GSI8.1) configurations described respectively by Storkey et al. (2017) and Ridley et al.

535 (2017). Coupling between the atmosphere-land and ocean-sea ice components is performed every hour using the OASIS3 MCT coupler.

The HadGEM3-GC31-MM model horizontal resolution is N216 for the atmosphere and land (~60 km in midlatitudes) and 0.25 degree (ORCA025) for the ocean and sea ice. Sea ice model resolution in the Arctic ranges between 9 km and 15.5 km with an average value of around 12.5 km. Meanwhile the HadGEM3-GC31-LL model

540 horizontal resolution is N96 for the atmosphere and land (~135 km in midlatitudes) and 1 degree (ORCA1) for the ocean and sea ice. Sea ice model resolution in the Arctic ranges between 37 km and 62.5 km with an average value of around 50.5 km. Both HadGEM3-GC31 models use 85 vertical levels in the atmosphere and the ocean components use 75 vertical levels with 8 levels in top 10m.

The sea ice model component is based upon version 5.1.2 of the CICE sea ice model of Hunke et al. (2015). The

545 CICE model uses a prognostic ice thickness distribution (ITD) with five thickness categories. The standard CICE elastic–viscous–plastic (EVP) rheology is used for ice dynamics (Hunke et al., 2015). The model uses the Bitz and Lipscomb (1999) multi-layer vertical thermodynamics with 4 layers of ice and 1 of snow.

Atmosphere-ice coupling is performed separately for each ice thickness category using the method of West et al., (2016). Surface exchanges over sea ice are calculated as part of the JULES surface exchange scheme; sea ice top-

550 layer temperature, thickness, and conductivity are passed to JULES from CICE with conductive and top-melting fluxes being passed back to CICE (see Ridley et al., 2017; West et al., 2016).

Radiation is calculated using CICE's "default" CCSM3 scheme (see Hunke et al., 2015) which uses separate albedos for visible (< 700 nm) and near-infrared (> 700 nm) wavelengths for both bare ice and snow. The scheme has been ported into JULES where the surface exchanges are calculated. Prognostic melt ponds are included using

555 the CICE topographic melt pond formulation of Flocco et al. (2010). Melt pond evolution is calculated in CICE with pond fraction and depth being passed through the coupler for use within the surface exchange scheme (albedo).

There are several minor differences between the LL and MM resolution version of HadGEM3-GC3.1, which are displayed in Table 2 of Roberts et al. (2019).

560

MRI-ESM2

The MRI-ESM2 model uses version 3.5 of the MRI-AGCM atmosphere/land model at TL159 (approximately 120 km) horizontal resolution with 80 vertical levels. The ocean and sea ice are modelled using version 4.4 of the

565 Meteorological Research Institute Community Ocean Model (MRI.COM; Tsujino et al., 2017) using a 1 degree resolution tri-polar grid.

The sea ice model component uses a prognostic ITD with 5 thickness categories and uses the elastic-viscous-plastic rheology of Hunke and Dukowicz (1997). Sea ice thermodunamics are performed following Mellor and Kantha (1989) using 1 layer of ice and a zero-layer snow scheme. Radiation is performed using the 'default' CICE

570 CCSM3 described in Hunke et al. (2015). Lateral melting is not modelled in MRI-COMv4 and so lateral melting is considered part of basal melting.

NorESM2-LM and NorESM2-MM

NorESM2 is built on the structure and many of the components in CESM2.1 as described in Danabasoglu et al.

575 (2019), but with varying degrees of modification as detailed by Seland et al (in prep). The NorESM2-LM and NorESM2-MM versions of the model differs in atmospheric horizontal resolution, 2 degree vs 1 degree nominal

resolution, respectively. In addition, some changes in tuning between the setups was necessary to have stable control climates.

The atmospheric model in NorESM2 (NorCAM6) is based on CAM6 but has undergone several modifications

580 both with respect to aerosol-radiation-cloud interaction (Kirkevåg et al. 2013; 2018) as well as changes in energy, momentum and flux. The land model CLM5 is close to the version in CESM2.1, and the river transport model Mosart is identical to the version found in CESM2.1. The ocean model BLOM and ocean-biogeochemistry model, HAMOCC, are upgraded versions of the components found in NorESM1 (Bentsen et al, Iversen et al, 2013). The ocean model and ocean– sea ice configuration are described in detail in Bentsen et al (in prep).

585 The sea ice model component is based upon version 5.1.2 of the CICE sea ice model of Hunke et al. (2015). The NorESM2-specific changes includes effects of wind drift of snow into ocean following Lecomte et al (2013) as described in Bentsen et al. (in prep), and a zenith angle-based time average of albedo.

The CICE model uses a prognostic ice thickness distribution (ITD) with five thickness categories. The standard CICE elastic–viscous–plastic (EVP) rheology is used for ice dynamics (Hunke et al., 2015). The model uses

590 mushy-layer thermodynamics and prognostic sea ice salinity (Turner et al., 2013) configured with 8 layers of ice and 3 of snow.

Radiation is calculated using the delta-Eddington scheme of Briegleb and Light (2007). Melt ponds are modelled on level, undeformed ice, as in Hunke et al. (2013).

595 UKESM1-0-LL

The UKESM1-0-LL model is the first version of the United Kingdom Earth System Model. UKESM1-0-LL uses the coupled climate model HadGEM3-GC31-LL as its physical core, with the following components interactively coupled: terrestrial carbon and nitrogen cycles, including dynamic vegetation and representation of agricultural land use change; ocean biogeochemistry (BGC) with prognostic diatom and non-diatom concentrations and a

600 unified troposphere-stratosphere chemistry model, tightly coupled to a multi-species modal aerosol scheme.

The model resolution – both vertical and horizontal – and details of the sea ice and ocean components of UKESM1-0-LL are otherwise identical to that of HadGEM3-GC31-LL described above.

The UKESM1-0-LL model is described further in Sellar et al. (2019).

605

Author Contributions

AK and EB defined the scope of the study. AK performed the model comparisons. AK wrote the paper, in collaboration with EB. DB, MB, DD, DF FM, LP, DS and NS provided text and comments. AK, DB, JB-D, MB,

610 SD, DD, S O'F, LP, J M-R, DS, NS, TT, HT, MV and KW provided processed data for the study.

Acknowledgements

Ann Keen and Ed Blockley were supported by the Joint UK BEIS/Defra Met Office Hadley Centre Climate

615 Programme (GA01101).

Ann Keen, Ed Blockley and Leandro Ponsoni were supported by the European Union's Horizon 2020 Research & Innovation programme through grant agreement no 727862 APPLICATE.

David Docquier was funded by the EU Horizon 2020 PRIMAVERA project, grant agreement no. 641727 (until
September 2019), and is currently funded by the EU Horizon 2020 OSeaIce project, under the Marie Sklodowska-
620   Curie grant agreement no. 834493.

David Schroeder was funded under the ACSIS and UKESM program (UK Natural Environment Research
Council)

Jens Boldingh Debernard was supported by the Research Council of Norway through INES (270061).

The ACCESS-CM2 CMIP6 submission was jointly funded through CSIRO and the Earth Systems and Climate
625   Change Hub of the Australian Government's National Environmental Science Program, with support from the
Australian Research Council Centre of Excellence for Climate System Science. The ACCESS model
simulations and data publication were supported by the National Computational Infrastructure (NCI).

We thank Dorotea Iovino for providing useful comments on the manuscript, and we thank all those who have
worked to develop the CMIP6 models and run the model integrations.

630

References

Adcroft, A., Anderson, W., Balaji, V., Blanton, C., Bushuk, M., Dufour, C. O., et al.: The GFDL global ocean
635   and sea ice model OM4.0: Model description and simulation features, Journal of Advances in Modeling Earth
Systems, 11, 3167– 3211, https://doi.org/10.1029/2019MS001726, 2019

Bathiany, S., van der Bolt, B., Williamson, M. S., Lenton, T. M., Scheffer, M., van Nes, E. H., and Notz, D.:
Statistical indicators of Arctic sea-ice stability – prospects and limitations, The Cryosphere, 10, 1631–1645,
https://doi.org/10.5194/tc-10-1631-2016, 2016

640   Bentsen, M., Bethke, I., Debernard, J. B., Iversen, T., Kirkevåg, A., Seland, Ø., Drange, H., Roelandt, C.,
Seierstad, I. A., Hoose, C., and Kristjánsson, J. E.: The Norwegian Earth System Model, NorESM1-M – Part 1:
Description and basic evaluation of the physical climate, Geosci. Model Dev., 6, 687–720,
https://doi.org/10.5194/gmd-6-687-2013, 2013.

Bentsen, M., Ilicak, M., Nummelin, A., Guo, C. and J.B.Debernard: Bergen Layered Ocean Model (BLOM):
645   Description and evaluation of global ocean–sea-ice experiments. To be submitted to Geosci. Mod. Dev.

Bitz, C. M., and Lipscomb, W. H.: An energy-conserving thermodynamic sea ice model for climate
study. J. Geophys. Res.–Oceans, 104:15669–15677, 1999

Briegleb, B. P., & Light, B.: A Delta-Eddington Mutiple Scattering Parameterization for Solar Radiation in the
Sea Ice Component of the Community Climate System Model (No. NCAR/TN-472+STR). University
650   Corporation for Atmospheric Research. doi:10.5065/D6B27S71, 2007

Danabasoglu, G., Lamarque, J. -F., Bachmeister, J., Bailey, D. A., DuVivier, A. K., Edwards, J., Emmons, L.
K., Fasullo, J., Garcia, R., Gettelman, A., Hannay, C., Holland, M. M., Large, W. G., Lawrence, D. M.,
Lenaerts, J. T. M., Lindsay, K., Lipscomb, W. H., Mills, M. J., Neale, R., Oleson, K. W., Otto-Bliesner, B.,
Phillips, A. S., Sacks, W., Tilmes, S., van Kampenhout, L., Vertenstein, M., Bertini, A., Dennis, J., Deser, C.,
655   Fischer, C., Fox-Kember, B., Kay, J. E., Kinnison, D., Kushner, P. J., Long, M. C., Mickelson, S., Moore, J. K.,
Nienhouse, E., Polvani, L., Rasch, P. J., Strand, W. G. The Community Earth System Model version 2
(CESM2). Manuscript submitted for publication to Journal of Advances in Modeling Earth Systems.

Dussin, R., B. Barnier and L. Brodeau: The making of Drakkar forcing set DFS5. DRAKKAR/MyOcean Report
01-04-16, LGGE, Grenoble, France, 2016

660   Fichefet, T., and Morales Maqueda, M.A.: Sensitivity of a global sea ice model to the treatment of ice thermodynamics and dynamics, Journal Geophs. Res., 102, 12609-12646, https://doi.org/10.1029/97JC00480, 1997.

Flocco, D., Schröder, D., Feltham, D. L., and Hunke, E. C.: Impact of melt ponds on Arctic sea ice simulations from 1990 to 2007, J. Geophys. Res., 117, C09032, https://doi.org/10.1029/2012JC008195, 2012

665   Gidden, M. J., Riahi, K., Smith, S. J., Fujimori, S., Luderer, G.,Kriegler, E., van Vuuren, D. P., van den Berg, M., Feng, L.,Klein, D., Calvin, K., Doelman, J. C., Frank, S., Fricko, O.,Harmsen, M., Hasegawa, T., Havlik, P., Hilaire, J., Hoesly, R.,Horing, J., Popp, A., Stehfest, E., and Takahashi, K.: Global emissions pathways under different socioeconomic scenarios for use in CMIP6: a dataset of harmonized emissions trajectories through the end of the century, Geosci. Model Dev., 12, 1443–1475, https://doi.org/10.5194/gmd-12-1443-2019, 2019.

670   Hawkins, E., and Sutton, R.: The Potential to Narrow Uncertainty in Regional Climate Predictions, *Bulletin of the American Meteorological Society* 90, 1095–1108, https://doi.org/10.1175/2009BAMS2607.1, 2009

Hazeleger, W., Wang, X., Severijns, C., Ştefănescu, S., Bintanja, R., Sterl, A., Wyser, K., Semmler, T., Yang, S., van den Hurk, B., van Noije, T., van der Linden, E., and van der Wiel, K.: EC-Earth V2.2: description and validation of a new seamless earth system prediction model, Climate Dynamics, 39, 2611–2629,

675   https://doi.org/10.1007/s00382-011-1228-5, 2012.

Held, I. M., Guo, H., Adcroft, A., Dunne, J. P., Horowitz, L. W., Krasting, J., et al.: Structure and performance of GFDL's CM4.0 climate model, Journal of Advances in Modeling Earth Systems, 11, https://doi.org/10.1029/2019MS001829, 2019.

Holland, M. M., Serreze, M. C., and Stroeve, J.: The sea ice mass budget of the Arctic and its future change as

680   simulated by coupled climate models, Clim. Dynam., 34,185–200, https://doi.org/10.1007/s00382-008-0493-4, 2010

Holmes, C., Holland, P., & Bracegirdle, T.: Compensating Biases and a Noteworthy Success in the CMIP5 Representation of Antarctic Sea Ice Processes. Geophysical Research Letters, 46 (8), 4299-4307. Retrieved from https://onlinelibrary.wiley.com/doi/abs/10.1029/2018GL081796 doi:10.1029/2018GL081796, 2019

685   Hunke, E. C., and Dukowicz, J. K.: An elastic-viscous-plastic model for sea ice dynamics. J. Phys. Oceanogr., 27:1849–1867, 1997

Hunke, E. C., Hebert, D. A., and Lecomte, O.: Level-ice melt ponds in the Los Alamos Sea Ice Model, CICE. Ocean Mod., 71:26–42, 2013

Hunke, E. C., Lipscomb, W. H., Turner, A. K., Jeffery, N., and Elliott, S.: CICE: the Los Alamos Sea Ice Model

690   Documentation and Software User's Manual Version 5.1, LA-CC-06-012, Los Alamos National Laboratory, Los Alamos, NM, 2015.

IPCC, 2019: Summary for Policymakers. In: IPCC Special Report on the Ocean and Cryosphere in a Changing Climate [H.-O. Pörtner, D.C. Roberts, V. Masson-Delmotte, P. Zhai, M. Tignor, E. Poloczanska, K. Mintenbeck, A. Alegría, M. Nicolai, A. Okem, J. Petzold, B. Rama, N.M. Weyer (eds.)]. In press.

695   Iversen, T., Bentsen, M., Bethke, I., Debernard, J. B., Kirkevåg, A., Seland, Ø., Drange, H., Kristjansson, J. E., Medhaug, I., Sand, M., and Seierstad, I. A.: The Norwegian Earth System Model, NorESM1-M – Part 2: Climate response and scenario projections, Geosci. Model Dev., 6, 389–415, https://doi.org/10.5194/gmd-6-389-2013, 2013.

Jahn, A., Kay, J. E., Holland, M. M., and Hall, D. M.: How predictable is the timing of a summer ice-free

700   Arctic? Geophys. Res. Lett., 2016GL070067, doi:10.1002/2016GL070067, 2016

Kirkevåg, A., Iversen, T., Seland, Ø., Hoose, C., Kristjánsson, J. E., Struthers, H., Ekman, A. M. L., Ghan, S.,

Griesfeller, J., Nilsson, E. D., and Schulz, M.: Aerosol–climate interactions in the Norwegian Earth System

Model – NorESM1-M, Geosci. Model Dev., 6, 207–244, https://doi.org/10.5194/gmd-6-207-2013, 2013.

Kirkevåg, A., Grini, A., Olivié, D., Seland, Ø., Alterskjær, K., Hummel, M., Karset, I. H. H., Lewinschal, A.,

705   Liu, X., Makkonen, R., Bethke, I., Griesfeller, J., Schulz, M., and Iversen, T.: A production-tagged aerosol

module for Earth system models, OsloAero5.3 – extensions and updates for CAM5.3-Oslo, Geosci. Model Dev.,

11, 3945–3982, https://doi.org/10.5194/gmd-11-3945-2018, 2018.

Kwok, R.: Arctic sea ice thickness, volume, and multiyear ice coverage: losses and coupled variability (1958–

2018), Environ. Res. Lett., 13 (2018), p. 105005, 2018

710   Large, W. G., and Yeager, S. G.: The global climatology of an interannually varying air-sea flux data set.

Climate Dynamics, 33, 341-364 (DOI: 10.1007/s00382-008-0441-3), 2009

Lavergne, T., Sørensen, A. M., Kern, S., Tonboe, R., Notz, D., Aaboe, S., Bell, L., Dybkjær, G., Eastwood, S.,

Gabarro, C., Heygster, G., Killie, M. A., Brandt Kreiner, M., Lavelle, J., Saldo, R., Sandven, S., and Pedersen,

L. T.: Version 2 of the EUMETSAT OSI SAF and ESA CCI sea-ice concentration climate data records, The

715   Cryosphere, 13, 49–78, https://doi.org/10.5194/tc-13-49-2019, 2019.

Lecomte, O., Fichefet, T., Vancoppenolle, M., Domine, F., Massonnet, F., Mathiot, P., Morin, S., and Barriat,

P.Y.: On the formulation of snow thermal conductivity in large scale sea ice models, J. Adv. Model. Earth Syst.,

5, 542– 557, doi:10.1002/jame.20039, 2013.

720   Long, M. C., Mickelson, S., Moore, J. K., Nienhouse, E., Polvani, L., Rasch, P. J., Strand, W. G. The

Community Earth System Model version 2 (CESM2). Manuscript submitted for publication to Journal of

Advances in Modeling Earth Systems

Madec, G.: NEMO Ocean ocean engine (Note du Pôle de modélisation, Institut Pierre-Simon Laplace (IPSL),

France, No 27, ISSN No 1288-1619), 2016.

725   Mahlstein, I., and Knutti, R.: September arctic sea ice predicted to disappear near 2C global warming above

present. J. Geophys. Res., 117 , D06104. doi:481 10.1029/2011JD016709, 2012

Massonnet, F., Fichefet, T., Goosse, H., Bitz, C. M., Philippon-Berthier, G., Holland, M. M., and Barriat, P.-Y.:

Constraining projections of summer Arctic sea ice. The Cryosphere, 6 (6), 1383-1394. doi: 10.5194/tc-6-1383-

2012, 2012

730   Maykut, G. A., and Untersteiner, N.: Some results from a time dependent thermodynamic model of sea ice. J.

Geophys. Res., 76:1550–1575, 1971

Melia, N., Haines, K., and Hawkins, E.: "Improved Arctic Sea Ice Thickness Projections Using Bias-Corrected

CMIP5 Simulations." *The Cryosphere* 9, 2237–51, https://doi.org/10.5194/tc-9-2237-2015, 2015

Mellor, G. L., and Kantha, L.: An ice-ocean coupled model, J. Geophys. Res., 94(C8), 10937–10954,

735   doi:10.1029/JC094iC08p10937, 1989

Notz, D., Jahn, A., Holland, M., Hunke, E., Massonnet, F., Stroeve, J., Tremblay, B., and Vancoppenolle, M.:

The CMIP6 Sea-Ice Model Intercomparison Project (SIMIP): understanding sea ice through climate-model

simulations, Geosci. Model Dev., 9, 3427–3446, https://doi.org/10.5194/gmd-9-3427-2016, 2016

740   Notz D., and Stroeve J.: Arctic sea ice loss directly follows cumulative anthropogenic CO_2 emissions, Science
        354, 2016

        Olason, E., and Notz, D.: Drivers of variability in Arctic sea-ice drift speed, Journal of Geophysical Research:
        Oceans, 119 (9), 5755-5775, 2014

        OSI-SAF: EUMETSAT Ocean and Sea Ice Satellite Application Facility, Global sea ice concentration climate
        data record 1979–2015 (v2.0), Norwegian and Danish Meteorological Institutes,
745   https://doi.org/10.15770/EUM_SAF_OSI_0008, 2017

        Pringle, D. J., Eicken, H., Trodahl, H. J., and Backstrom, L. G. E.: Thermal conductivity of landfast Antarctic
        and Arctic sea ice, J. Geophys. Res., 112, C04017, https://doi.org/10.1029/2006JC003641, 2007

        Rampal, P., J. Weiss, C. Dubois and J.-M. Campin, 2011: IPCC climate models do not capture Arctic sea ice
        drift acceleration: Consequences in terms of projected sea ice thinning and decline. Journal of Geophysical
750   Research: Oceans, 116 (C8), C00D07, doi:10.1029/2011JC007110.

        Rayner, N. A., Parker, D. E., Horton, E. B., Folland, C. K., Alexander, L. V., Rowell, D. P., Kent, E. C., and
        Kaplan, A.: Global analyses of sea surface temperature, sea ice, and night marine air temperature since the late
        nineteenth century, J. Geophys. Res., 108, 4407 https://doi.org/10.1029/2002JD002670, 2003

        Ridley, J. K., Blockley, E. W., Keen, A. B., Rae, J. G. L., West, A. E., and Schroeder, D.: The sea ice model
755   component of HadGEM3-GC3.1, Geosci. Model Dev., 11, 713–723, https://doi.org/10.5194/gmd-11-713-2018,
        2018.

        Roberts, M. J., Baker, A., Blockley, E. W., Calvert, D., Coward, A., Hewitt, H. T., Jackson, L. C., Kuhlbrodt,
        T., Mathiot, P., Roberts, C. D., Schiemann, R., Seddon, J., Vannière, B., and Vidale, P. L.: Description of the
        resolution hierarchy of the global coupled HadGEM3-GC3.1 model as used in CMIP6 HighResMIP
760   experiments, Geosci. Model Dev., 12, 4999–5028, https://doi.org/10.5194/gmd-12-4999-2019, 2019.

        Rosenblum, E., and Eisenman, I., Sea Ice Trends in Climate Models Only Accurate in Runs with Biased Global
        Warming. J. Climate, 30, 6265–6278, https://doi.org/10.1175/JCLI-D-16-0455.1, 2017

        Rousset, C., Vancoppenolle, M., Madec, G., Fichefet, T., Flavoni, S., Barthélemy, A., Benshila, R., Chanut, J.,
        Levy, C., Masson, S., and Vivier, F.: The Louvain-La-Neuve sea ice model LIM3.6: global and regional
765   capabilities, Geosci. Model Dev., 8, 2991–3005, https://doi.org/10.5194/gmd-8-2991-2015, 2015.

        Schroeder, D., Feltham, D. L., Tsamados, M., Ridout, A. and Tilling, R.: New insight from CryoSat-2 sea ice
        thickness for sea ice modelling. The Cryosphere. ISSN 1994-0424, https://doi.org/10.5194/tc-13-125-2019,
        2019

        Seland et al.: The Norwegian Earth System Model, NorESM2. Description, updates and evaluation from CMIP
770   DECK and historical simulations. To be submitted to Geosci. Mod. Dev.

        Sellar, A. A., Jones, C. G., Mulcahy, J., Tang, Y., Yool, A., Wiltshire, A., et al: UKESM1: Description and
        evaluation of the UK Earth System Model. Journal of Advances in Modeling Earth Systems, 11.
        https://doi.org/10.1029/2019MS001739 , 2019

        SIMIP Community: Arctic Sea Ice in CMIP6. Geophysical Research Letters, in prep, 2020
775   Smith, B., Wårlind, D, Arneth, A., Hickler, T., Leadley, P, Siltberg, J., and Zaehle, S.: Implications of
        incorporating N cycling and N limitations on primary production in an individual-based dynamic vegetation
        model, Biogeosciences, 11, 2047-2054, https://doi.org/10.5194/bg-11-2027-2014, 2014.

Storkey, D., Blaker, A. T., Mathiot, P., Megann, A., Aksenov, Y., Blockley, E. W., Calvert, D., Graham, T., Hewitt, H. T., Hyder, P., Kuhlbrodt, T., Rae, J. G. L., and Sinha, B.: UK Global Ocean GO6 and GO7: a

780   traceable hierarchy of model resolutions, Geosci. Model Dev., 11, 3187–3213, https://doi.org/10.5194/gmd-11-3187-2018, 2018.

Stroeve, J., A. Barrett, M. Serreze, and A. Schweiger: Using records from submarine, aircraft and satellites to evaluate climate model simulations of Arctic sea ice thickness. Cryosphere, 8, 1839–1854, https://doi.org/10.5194/tc-8-1839-2014, 2014

785   Stroeve, J., and Notz, D.: Insights on past and future sea-ice evolution from combining observations and models. Glob. Planet Change, 135, 119-132. doi:10.1016/j.gloplacha.2015.10.011, 2015

Swart, N. C., Cole, J. N. S., Kharin, V. V., Lazare, M., Scinocca, J. F., Gillett, N. P., Anstey, J., Arora, V., Christian, J. R., Hanna, S., Jiao, Y., Lee, W. G., Majaess, F., Saenko, O. A., Seiler, C., Seinen, C., Shao, A., Sigmond, M., Solheim, L., von Salzen, K., Yang, D., and Winter, B.: The Canadian Earth System Model

790   version 5 (CanESM5.0.3), Geosci. Model Dev., 12, 4823–4873, https://doi.org/10.5194/gmd-12-4823-2019, 2019.

Tandon, N.F. et al., 2018: Reassessing Sea Ice Drift and Its Relationship to Long-Term Arctic Sea Ice Loss in Coupled Climate Models. Journal of Geophysical Research: Oceans, 123 (6), 4338–4359, doi:10.1029/2017jc013697.

795   Titchner, H. A., and N. A. Rayner: The Met Office Hadley Centre sea ice and sea surface temperature data set, version 2: 1. Sea ice concentrations, J. Geophys. Res. Atmos., 119, 2864-2889, doi:10.1002/2013JD020316, 2014

Tsamados, M., Feltham, D. L., and Wilchinsky, A. V.: Impact of a new anisotropic rheology on simulations of Arctic sea ice, J. Geophys. Res., 118, 91–107, https://doi.org/10.1029/2012JC007990, 2013

800   Tsujino, H., Nakano, H., Sakamoto, K., Urakawa, S., Hirabara, M., Ishizaki, H., and Yamanaka, G.: Reference Manual for the Meteorological Research Institute Community Ocean Model version 4 (MRI.COMv4), doi:10.11483/mritechrepo.80, 2017

Turner, A. K., Hunke, E. C., and Bitz, C. M.: Two modes of sea-ice gravity drainage: a parameterization for large-scale modeling. J. Geophys. Res., 118:2279–2294, doi:10.1002/jgrc.20171, 2013.

805   van den Hurk, B., Viterbo, P., Beljaars, A., and Betts, A.: Offline validation of the ERA40 surface scheme, https://doi.org/10.21957/9aoaspz8, 2000.

Walters, D. N., Best, M. J., Bushell, A. C., Copsey, D., Edwards, J. M., Falloon, P. D., Harris, C. M., Lock, A. P., Manners, J. C., Morcrette, C. J., Roberts, M. J., Stratton, R. A., Webster, S., Wilkinson, J. M., Willett, M. R., Boutle, I. A., Earnshaw, P. D., Hill, P. G., MacLachlan, C., Martin, G. M., Moufouma-Okia, W., Palmer, M. D.,

810   Petch, J. C., Rooney, G. G., Scaife, A. A., and Williams, K. D.: The Met Office Unified Model Global Atmosphere 3.0/3.1 and JULES Global Land 3.0/3.1 configurations, Geosci. Model Dev., 4, 919–941, https://doi.org/10.5194/gmd-4-919-2011, 2011.

Wang, X., J. Key, R. Kwok, and J. Zhang: Comparison of Arctic sea ice thickness from satellites, aircraft, and PIOMAS data. Remote Sens., 8, 713, https://doi.org/10.3390/rs8090713, 2016

815

West, A. E., McLaren, A. J., Hewitt, H. T., and Best, M. J.: The location of the thermodynamic atmosphere–ice interface in fully coupled models – a case study using JULES and CICE, Geosci. Model Dev., 9, 1125–1141, https://doi.org/10.5194/gmd-9-1125-2016, 2016.

Winton, M.: Do climate models underestimate the sensitivity of northern hemisphere sea ice cover? J. Clim., 24
820   (15), 3924-3934, 2011

Williams, K. D., Copsey, D., Blockley, E. W., Bodas-Salcedo, A., Calvert, D., Comer, R., et al.: The Met Office Global Coupled model 3.0 and 3.1 (GC3.0 and GC3.1) configurations. Journal of Advances in Modeling Earth Systems, 10, 357–380, https://doi.org/10.1002/2017MS001115, 2017

Zhang, J. and Rothrock, D. A.: Modeling global sea ice with a thickness and enthalpy distribution model in
825   generalized curvilinear coordinates, Mon. Weather Rev., 131, 681–697, 2003

Zhao, M., Golaz, J.-C., Held, I. M., Guo, H., Balaji, V., Benson, R., et al.: The GFDL global atmosphere and land model AM4.0/LM4.0: 1. Simulation characteristics with prescribed SSTs, Journal of Advances in Modeling Earth Systems, 10, 691– 734, https://doi.org/10.1002/2017MS001208, 2018.

830

835

840

845

Tables

850

Model Name	Modelling Centre	No of integrations		Notes
		Hist	SSP58.5	
HadGEM3-GC31-LL	Met Office	4	4	
HadGEM3-GC31-MM	Met Office	4	4	
UKESM1-0-LL	Met Office	12	5	
EC-Earth-3	UCLouvain/AEMET	1	1	
EC-Earth3-Veg	UCLouvain/SMHI	1	1	Missing terms: lateral melt and dynamics
MRI-ESM2	MRI	5	1	No explicit lateral melt term
CESM2-CAM	NCAR	11	2	
CESM2-WACCM	NCAR	3	2	
GFDL-CM4	GFDL	1	1	No explicit lateral melt term
GFDL-ESM4	GFDL	1	1	No explicit lateral melt term
CSIRO_ARCCSS_ACCESS-CM2	CSIRO	1	1	
NorESM2-LM	Met Norway	3	1	
NorESM2-MM	Met Norway	1	1	
CanESM5	ECCC	3	3	Missing terms: frazil, lateral melt, evapsubl, dynamics.
NEMOCICE_CORE_default	CPOM	1		Forced ocean-ice model (so no scenario data)
NEMOCICE_CORE_CPOM-CICE	CPOM	1		
NEMOCICE_DFS5.2_CPOM-CICE	CPOM	1		

***Table 1**: List of models and modelling centres participating in this study. Where two modelling centres are shown, the 1st analysed the model outputs, and the 2nd performed the model integrations.*

	UKESM1-0-LL	HadGEM3-GC31-LL	HadGEM3-GC31-MM	EC-Earth3	EC-Earth3-Veg	ACCESS-CM2	MRI-ESM2
Components, resolution:							
Sea ice model component (configuration)	CICE 5.1.2 (GSI8.1)	CICE 5.1.2 (GSI8.1)	CICE 5.1.2 (GSI8.1)	LIM3	LIM3	CICE 5.1.2 (GSI8.1)	MRI.COM 4.4
Sea ice model resolution	1° (ORCA1)	1° (ORCA1)	0.25° (ORCA025)	1° (ORCA1)	1° (ORCA1)	1°	1° (lon) x 0.3-0.5° (lat)
Ocean model component (configuration)	NEMO 3.6 (GO6)	NEMO 3.6 (GO6)	NEMO 3.6 (GO6)	NEMO 3.6	NEMO 3.6	MOM 5.1 (ACCESS-OM)	MRI.COM 4.4
Ocean model resolution	1° (ORCA1)	1° (ORCA1)	0.25° (ORCA025)	1° (ORCA1)	1° (ORCA1)	1°	1° (lon) x 0.3-0.5° (lat)
Atmosphere model component (configuration)	MetUM (GA7.1)	MetUM (GA7.1)	MetUM (GA7.1)	IFS cycle 36r4	IFS cycle 36r4	MetUM (GA7.1)	MRI-AGCM 3.5
Atmosphere model resolution	135 km (N96)	135 km (N96)	60 km (N216)	100 km (T255L91)	100 km (T255L91)	135 km (N96)	120 km (TL159)
Sea ice model specifics:							
Rheology	EVP	EVP	EVP	EVP	EVP	EVP	EVP
(ITD)	Prognostic	Prognostic	Prognostic	Prognostic	Prognostic	Prognostic	Prognostic
No of thickness categories	5	5	5	5	5	5	5
Radiation scheme	Dual band (CCSM3)	Dual band (CCSM3)	Dual band (CCSM3)	Broadband	Broadband	Dual band (CCSM3)	Dual band (CCSM3)
Melt-ponds	Prognostic F12	Prognostic F12	Prognostic F12	None	None	Prognostic F12	Parameterised
Thermodynamics	BL99	BL99	BL99	BL99	BL99	BL99	MK89
No of ice (snow) layers	4 (1)	4 (1)	4 (1)	2 (1)	2 (1)	4 (1)	1 (0)
Minimum lead fraction	None	None	None	0.003	0.003	None	0.02
Minimum frazil thickness	5 cm	5 cm	5 cm	10 cm	10 cm	5 cm	20 cm
Coupling, time-stepping:							
Sea ice model time-step	30 mins	30 mins	20 mins	45 mins	45 mins	30 mins	30 mins
Ice-ocean coupling frequency	30 mins	30 mins	20 mins	45 mins	45 mins	30 mins	30 mins
Ice-atmosphere coupling frequency	20 mins (180 mins)	20 mins (180 mins)	20 mins (60 mins)	45 mins	46 mins	20 mins (180 mins)	60 mins

Table 2: *Relevant information for all the CMIP6 models used in this study including a summary of the model subcomponents and resolution, along with details of several key physical aspects of the sea ice subcomponents. For thermodynamics: T13 denotes the mushy-layer scheme of Turner et al. (2013), whilst BL99 and MK89 denote fixed salinity-profile schemes of Bitz and Lipscomb (1999) and Mellor and Kantha (1989), respectively. For prognostic melt-ponds: F12 denotes the 'topographic' scheme of Flocco et al. (2012), whilst H13 denotes the 'level ice' scheme of Hunke et al. (2013). For rheology: EVP is the Elastic-Viscous-Plastic scheme of Hunke and Dukowicz (1997).*

	GFDL-CM4	GFDL-ESM4	CanESM5	CESM2-CAM	CESM2-WACCM	NorESM-LM	NorESM-MM
Components, resolution:							
Sea ice model component (configuration)	SIS2	SIS2	LIM2	CICE 5.1.2	CICE 5.1.2	CICE 5.1.2	CICE 5.1.2
Sea ice model resolution	0.25°	0.5°	1° (ORCA1)	1° (gx1)	1° (gx1)	1° (tn1v4)	1° (tn1v4)
Ocean model component (configuration)	MOM6 (OM4.0)	MOM6 (OM4.0)	NEMO 3.4.1	POP 2.0.1	POP 2.0.1	BLOM	BLOM
Ocean model resolution	0.25°	0.5°	1° (ORCA1)	1° (gx1)	1° (gx1)	1° (tn1v4)	1° (tn1v4)
Atmosphere model component (configuration)	GFDL-AM (AM4.0)	GFDL-AM (AM4.0)	CanAM	CAM 6	CAM 6	NorCAM6	NorCAM6
Atmosphere model resolution	100 km	100 km	2.8° (T63)	0.9° (lon) x 1.25° (lat)	0.9° (lon) x 1.25° (lat)	0.9° (lon) x 1.25° (lat)	1.9° (lon) x 2.5° (lat)
Sea ice model specifics:							
Rheology	EVP	EVP	EVP	EVP	EVP	EVP	EVP
(ITD)	Prognostic	Prognostic	Diagnostic	Prognostic	Prognostic	Prognostic	Prognostic
No of thickness categories	5	5	1	5	5	5	5
Radiation scheme	delta-Eddington	delta-Eddington	Multi-band	delta-Eddington	delta-Eddington	delta-Eddington	delta-Eddington
Melt-ponds	Parameterised	Parameterised	Parameterised	Prognostic H13	Prognostic H13	Prognostic H13	Prognostic H13
Thermodynamics	BL99	BL99	0-layer	T13	T13	T13	T13
No of ice (snow) layers	4 (1)	4 (1)	N/A	8 (3)	8 (3)	8 (3)	8 (3)
Minimum lead fraction	None	None	1.00E-06	None	None	None	None
Minimum frazil thickness	None	None	5 cm	5 cm	5 cm	5 cm	5 cm
Coupling, time-stepping:							
Sea ice model time-step	20 mins	20 mins	60 mins	30 mins	30 mins	30 mins	30 mins
Ice-ocean coupling frequency	60 mins	60 mins	60 mins	30 mins	30 mins	30 mins	30 mins
Ice-atmosphere coupling frequency	20 mins	20 mins	180 mins	60 mins	60 mins	30 mins	30 mins

	CPOM_NEMOCICE_CORE_default	CPOM_NEMOCICE_CORE_CPOM-CICE	CPOM_NEMOCICE_DFS5.2_CPOM-CICE	HadGEM3-GC3.1-LL
Atmospheric forcing:				
Atmospheric forcing dataset	CORE II	CORE II	DFS5.2	MetUM coupled
Atmospheric forcing resolution	~200km	~200km	~80km	~135km (N96)
Atmospheric forcing frequency	6 hourly	6 hourly	6 hourly	3 hourly
Sea ice model physics:				
Rheology	EVP	EAP	EAP	EVP
Sea ice conductivity	"default" (Maykut and Untersteiner, 1971)	"bubby brine" (Pringle et al., 2007)	"bubby brine" (Pringle et al., 2007)	"default" (Maykut and Untersteiner, 1971)
Sea ice emissivity	0.95	0.976	0.976	0.95
Melt pond max fraction (rfracmax)	85%	50%	50%	85%
Blown snow scheme	None	Schroeder et al.	Schroeder et	None

860

Table 3: *Relevant information describing the CPOM NEMO-CICE forced models used in this study. Including details of the atmospheric forcing datasets used and the changes in the CICE sea ice physics used in the different simulations. Also included is the HadGEM3-GC3.1-LL model for reference. All physics options not included in this table – including those shown in Table 2 above – are identical to the HadGEM3-GC3.1-LL model.*
865 *CORE II is the CORE2 surface forcing data set of Large and Yeager (2009), whilst DFS5.2 is the Drakkar forcing set of Dussin et al. (2016). For rheology: EVP is the Elastic-Viscous-Plastic scheme of Hunke and Dukowicz (1997); EAP is the Elastic-Anisotropic-Plastic scheme of Tsamados et al (2013). The melt-pond max fraction term (rfracmax) determines the maximum fraction of melt-water added to the ponds within the Flocco et al. (2012) 'topographic' prognostic melt-pond scheme.*

870
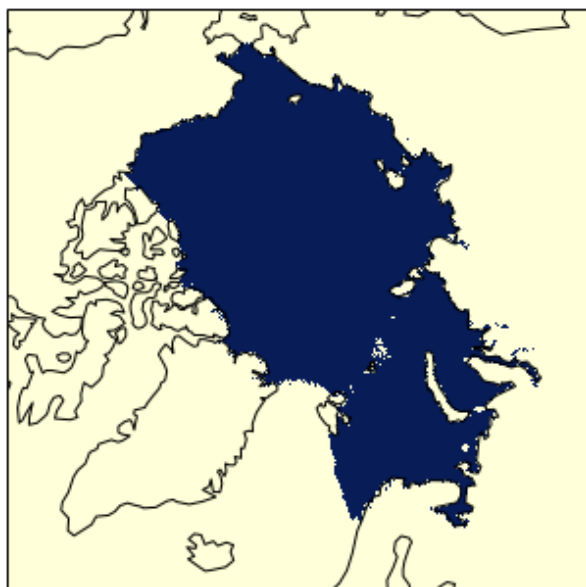
Figures

875

Figure 1: Analysis domain. The domain is defined using the NSIDC Arctic regional masks (https://nsidc.org/data/polar-stereo/tools_masks.html#region_masks), where we include the following regions: Central Arctic Ocean, Beaufort Sea, Chukchi Sea, East Siberian Sea, Laptev Sea, Kara Sea and Barents Sea.

880

885
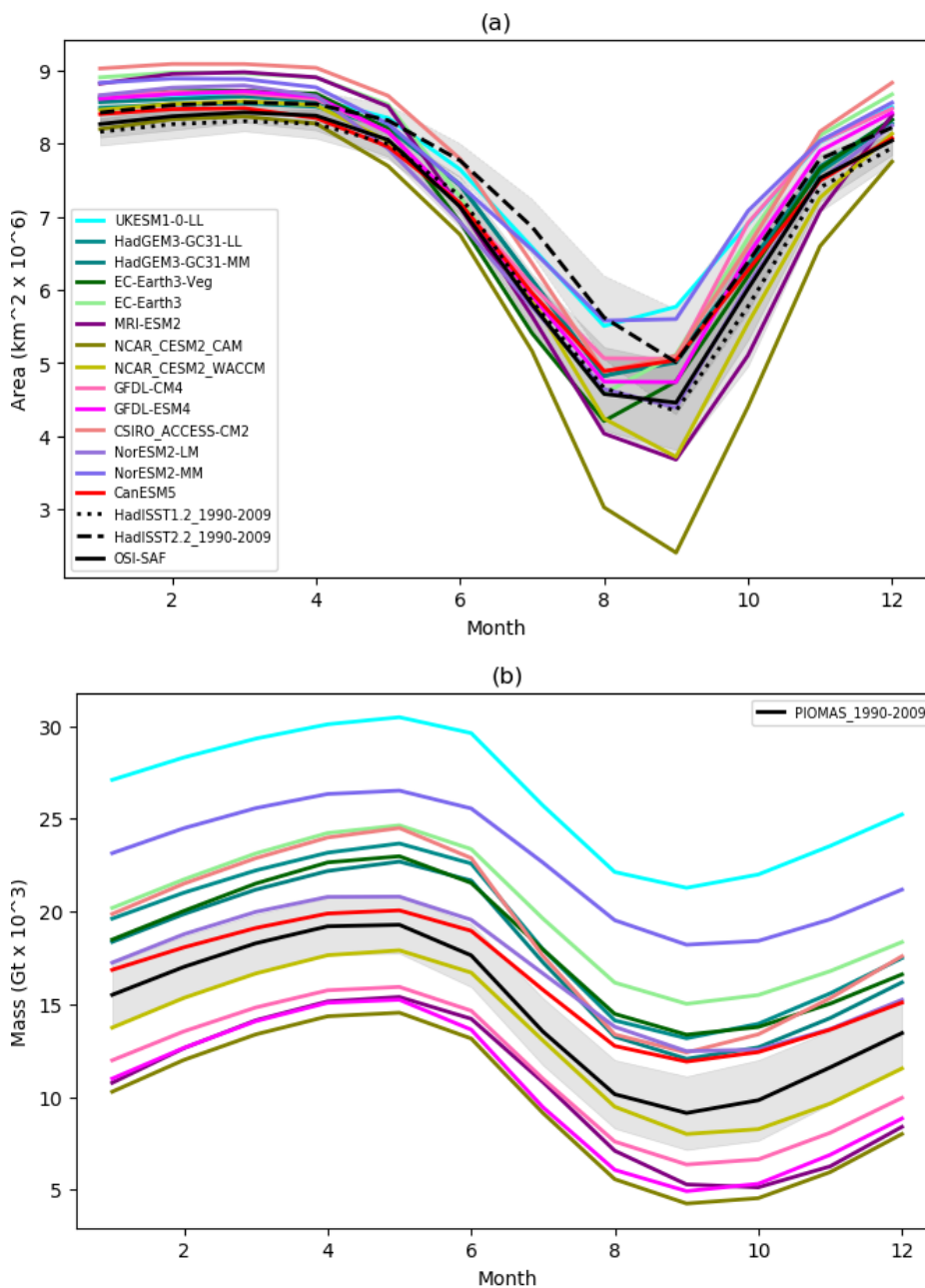
Figure 2: Seasonal cycles of (a) ice area and (b) ice mass for the reference period 1990-2009, for the
CMIP6 models. Where more than one model integration is available, the values are ensemble means.
890   Also shown is data for the same periods for (a) the HadISST1.2 (Rayner et al., 2003), HadISST.2.2
(Titchner and Rayner, 2014) and OSI-SAF (OSI-SAF, 2017) observational datasets, and (b) PIOMAS
reanalysis (Zhang and Rothrock, 2003) for the same period. The shaded regions show +/- 1 standard
deviation in the monthly values.

895
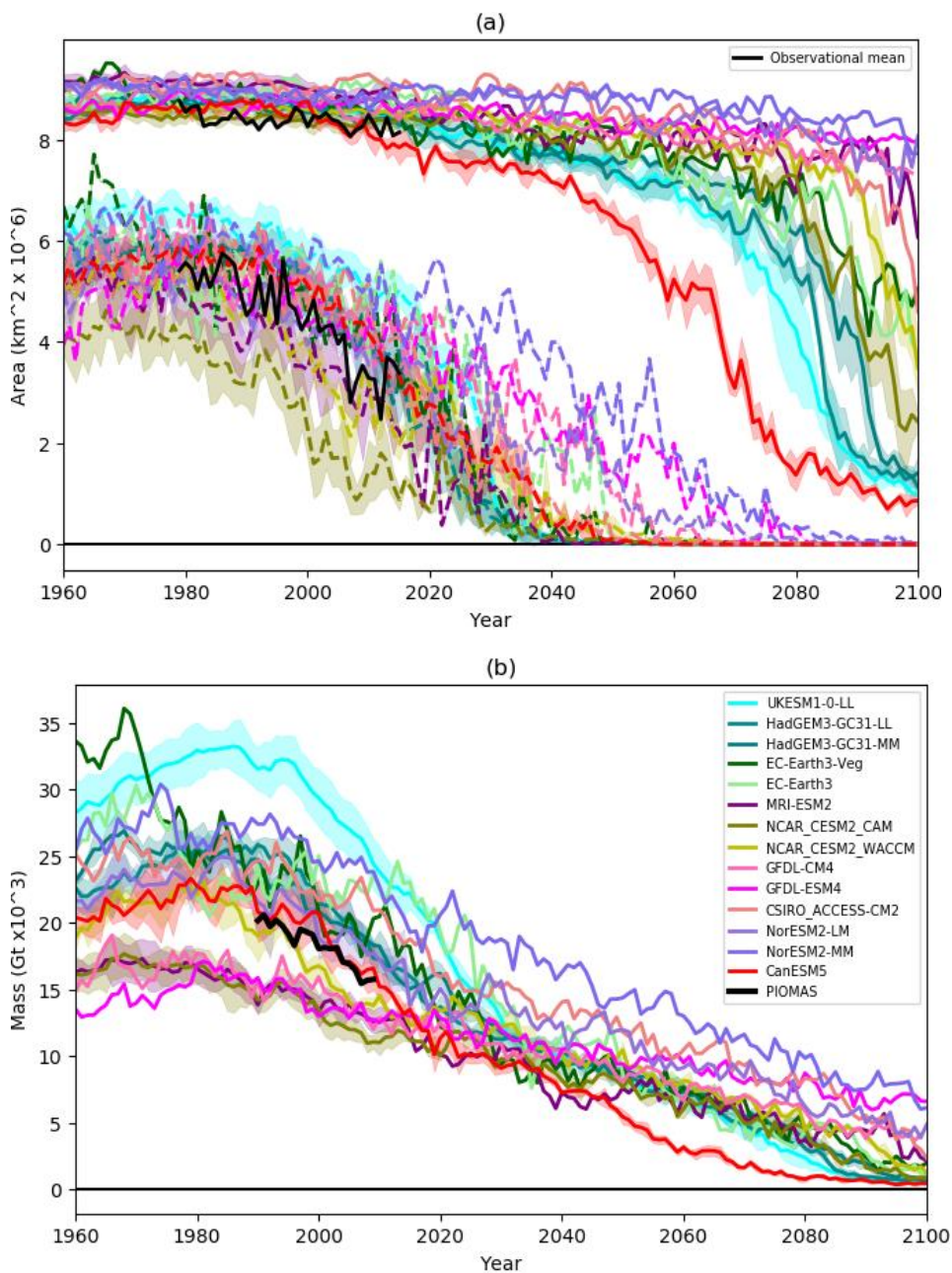
Figure 3: Evolution of (a) March and September ice area and (b) March ice mass for the CMIP6 models. Also shown is (a) the mean of the HadISST1.2 (Rayner et al., 2003), HadISST.2.2 (Titchner and Rayner, 2014) and OSI-SAF (OSI-SAF, 2017) observational datasets, and (b) the PIOMAS reanalysis (Zhang and Rothrock, 2003).

900
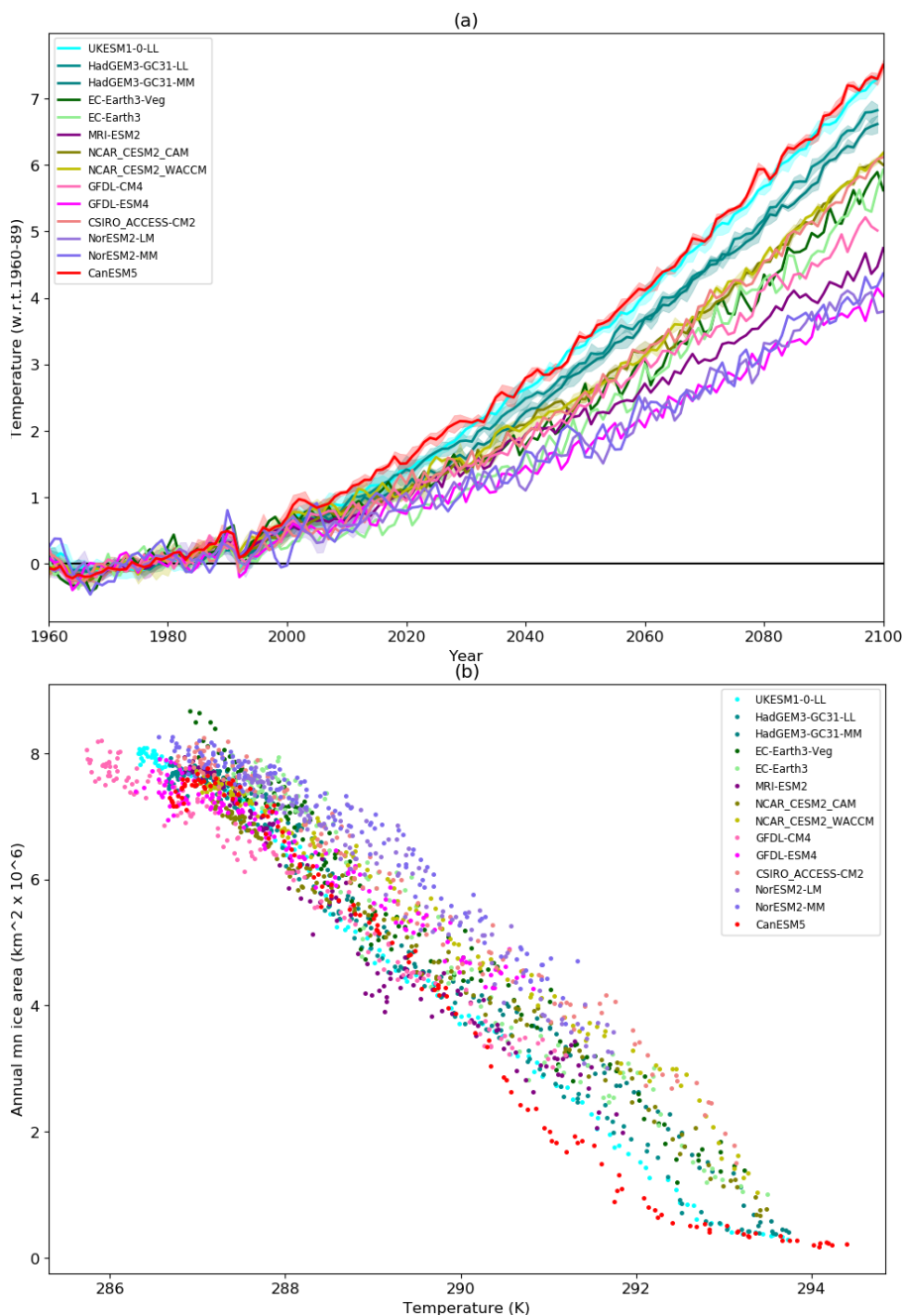
905

Figure 4: (a) Evolution of annual-mean global-mean near-surface temperature. Values are relative to 1960-89 for each model. (b) Scatter plot of annual mean ice area vs annual-mean global-mean near-surface temperature for each model.

910
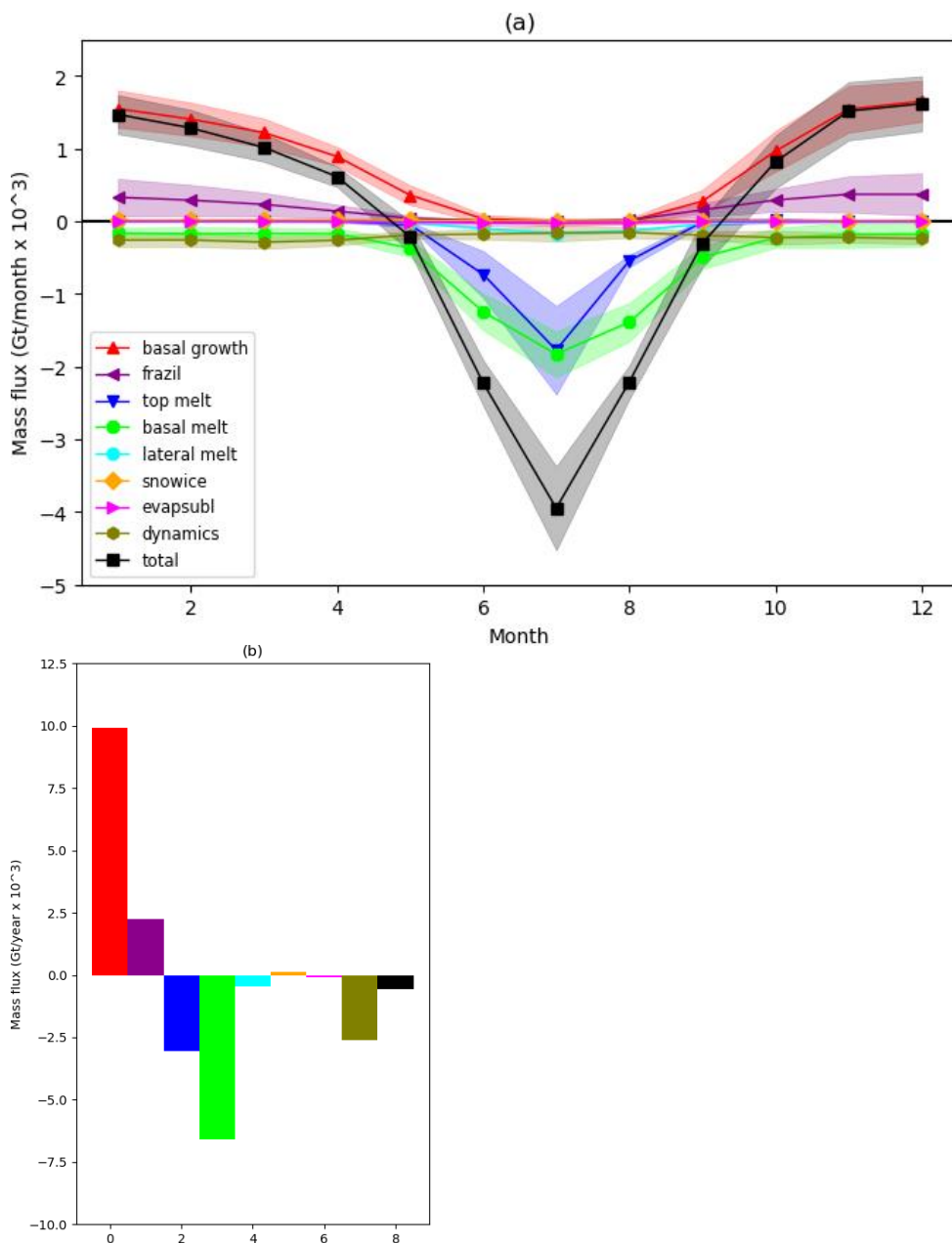
Figure 5: Components of the Arctic sea ice mass budget for the multi-model mean. Values are summed over the region shown in Fig. 1, for the period 1960-89. For each budget component, values are calculated by averaging the ensemble mean for each model with a non-zero value of the component. (a) Seasonal cycle of monthly mean values, (b) annual mean values. The shaded regions show +/- 1 standard deviation in the modelled values.

915

920
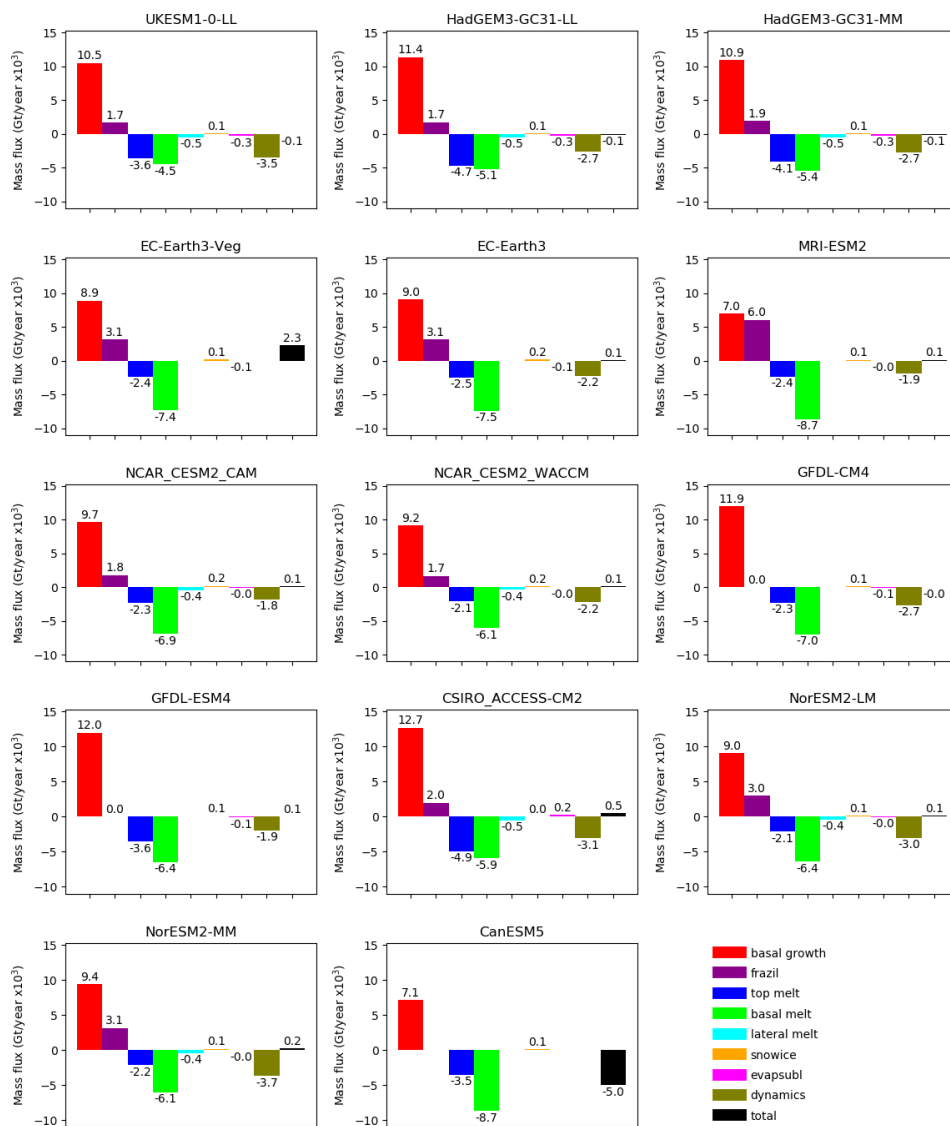
925

Figure 6: Components of the annual mean Arctic sea ice mass budget for each model. Values are summed over the region shown in Fig. 1, for the period 1960-89. Note that the total will only be close to zero for models with no missing budget terms.
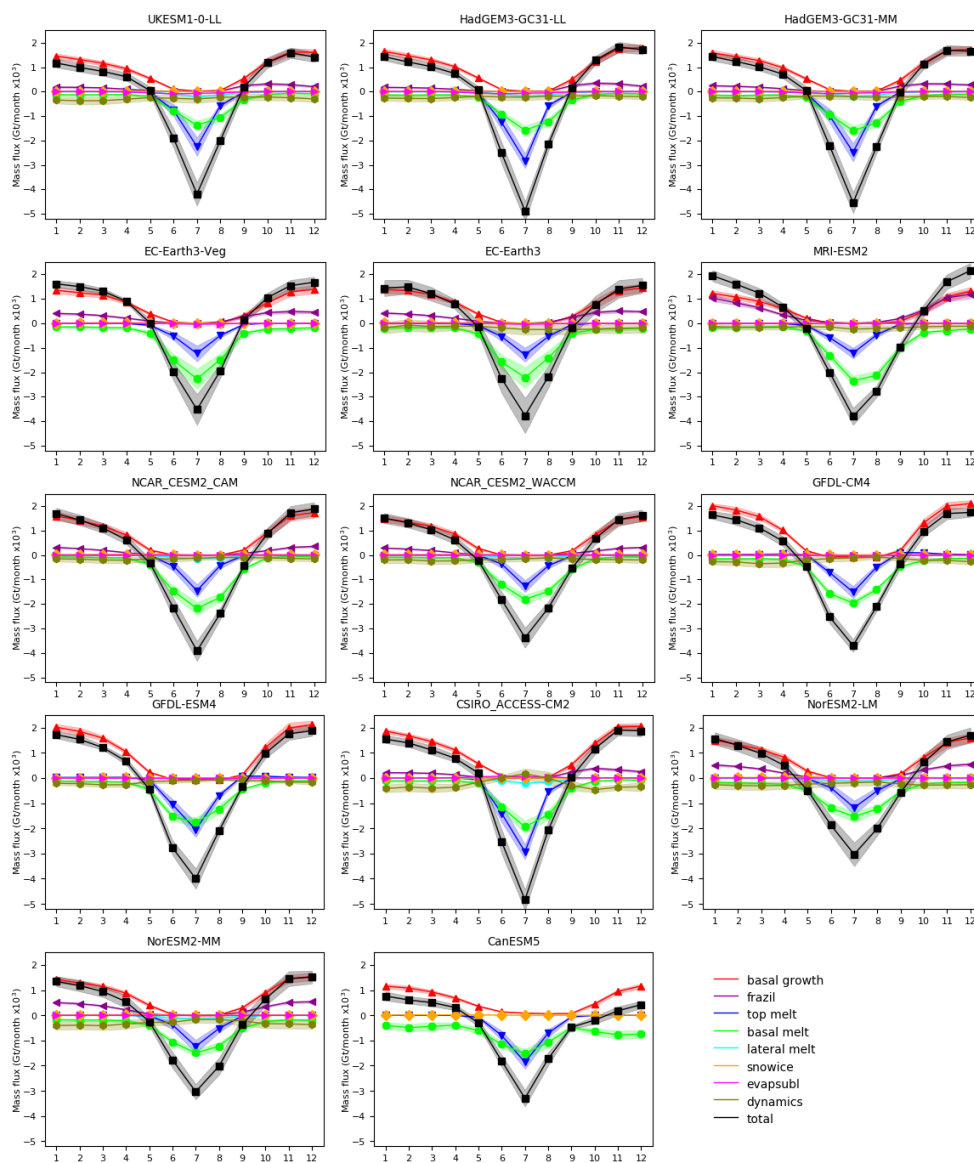
930

Figure 7: Seasonal cycles of monthly mean components of the Arctic sea ice mass budget for each model. Values are summed over the region shown in Fig. 1, for the period 1960-89.
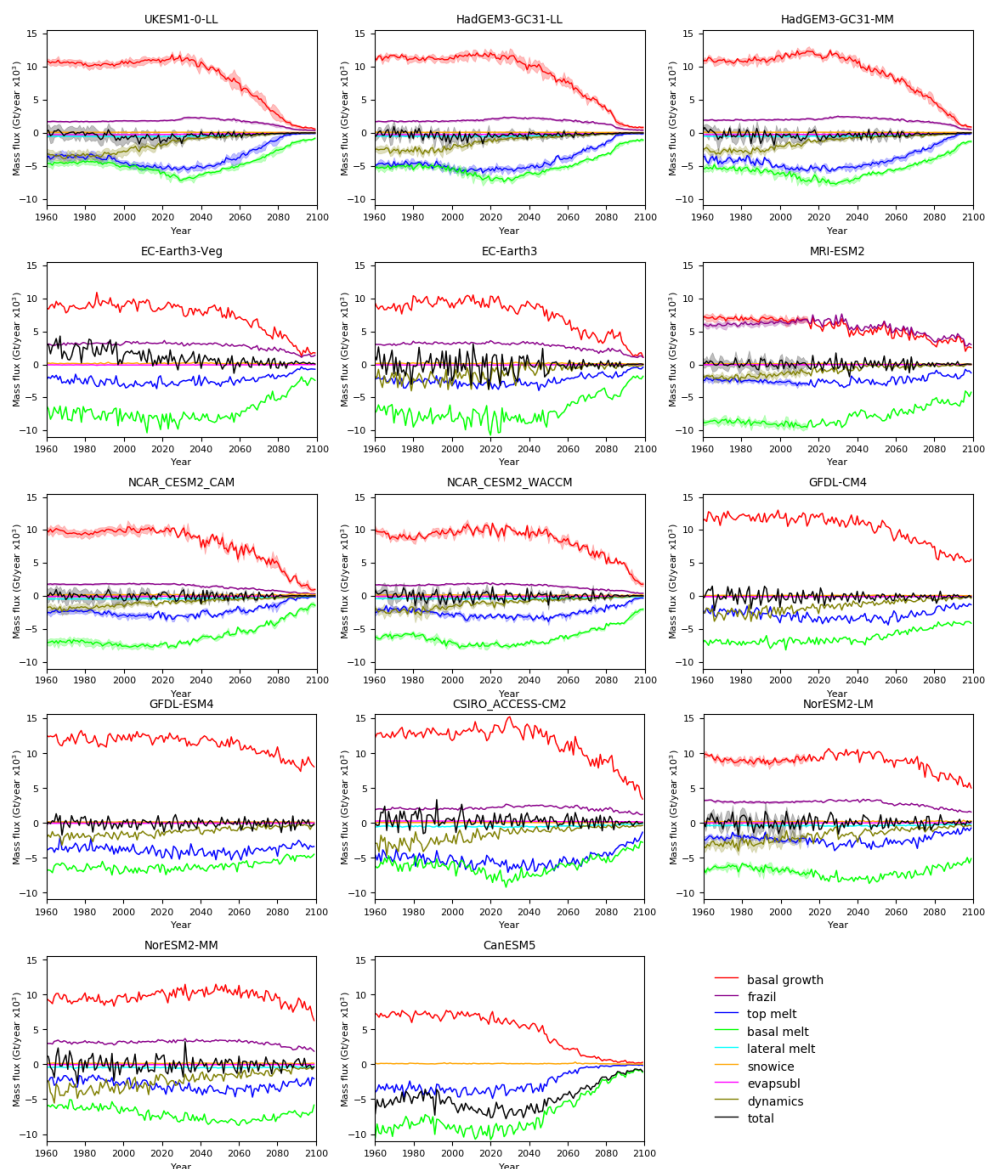
Figure 8: Evolution of annual mean components of the Arctic sea ice mass budget for each model. Values are summed over the region shown in Fig. 1.

935

940
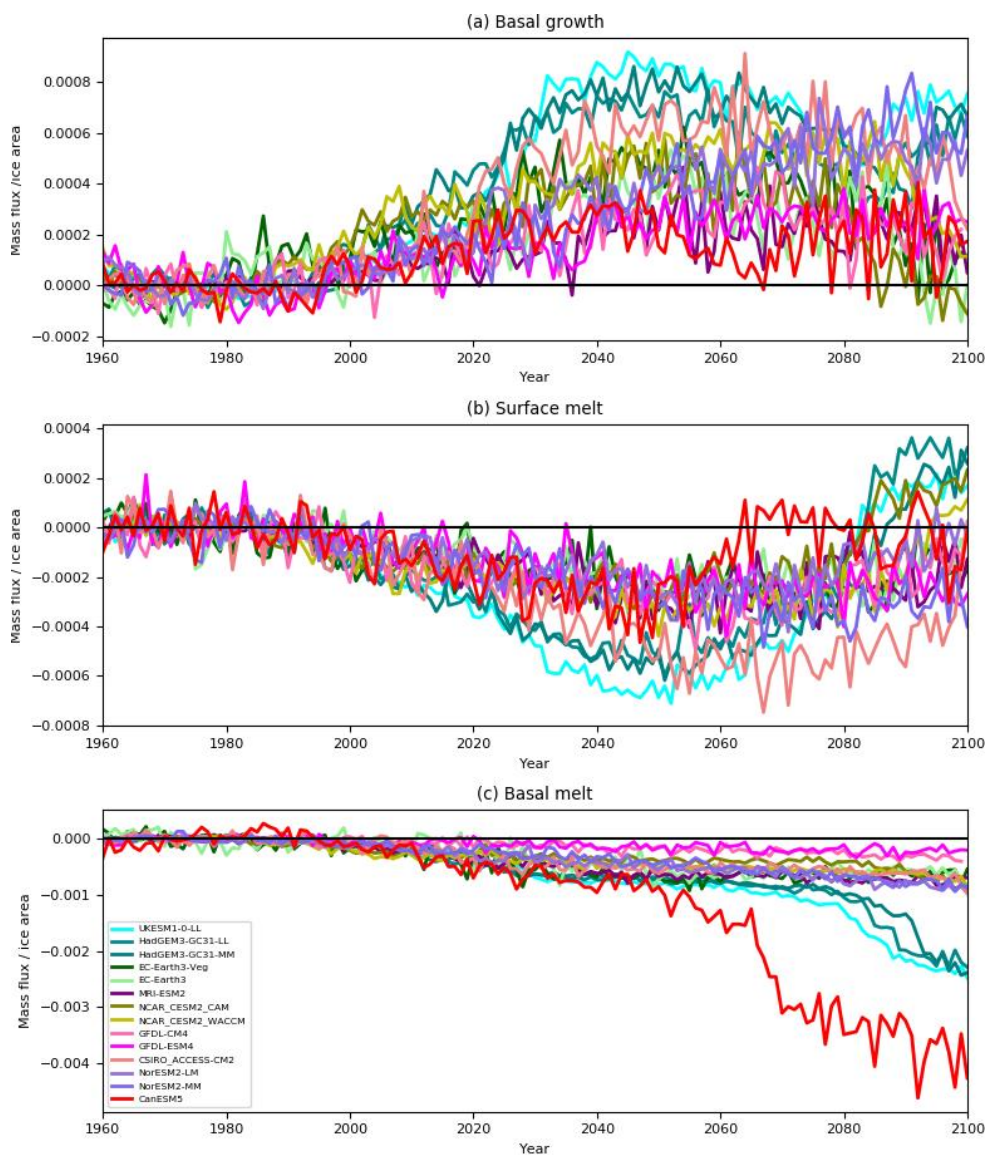
945

Figure 9: Evolution of anomalies relative to the 1960-89 mean of selected annual mean components of the Arctic sea ice mass budget, per unit area of the remaining ice, for all the models. Values are summed over the region shown in Fig. The units are $Gt \times 10^3 \ year^{-1} \ km^{-2}$. (a) Basal growth (b) Top Melt (c) Basal melt

950
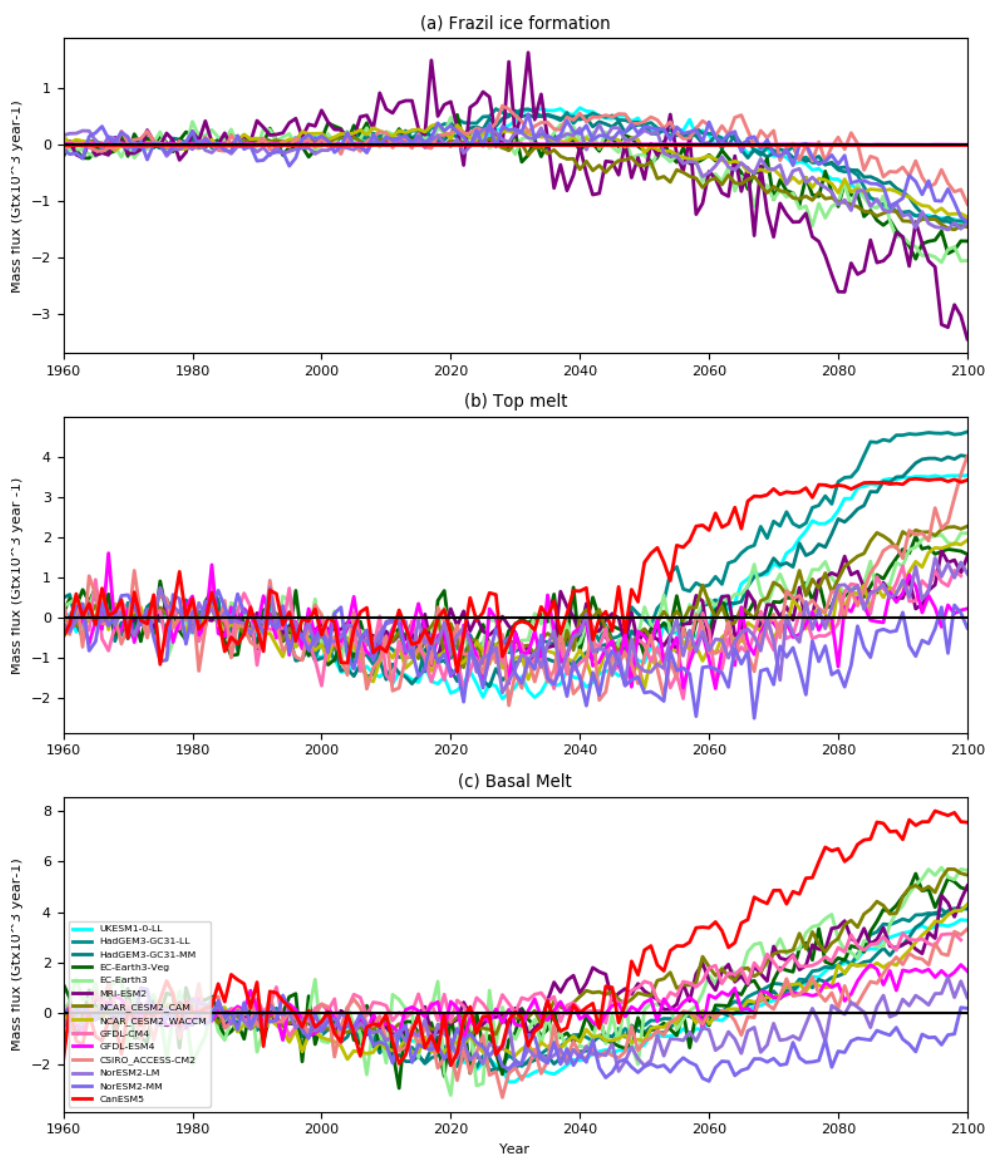
Figure 10: Evolution anomalies relative to the 1960-89 mean of selected annual mean components of the Arctic sea ice mass budget for all the models. Values are summed over the region shown in Fig. 1. The units are Gtx10^3 year^{-1}. (a) Frazil ice formation (b) Top Melt (c) Basal melt

955
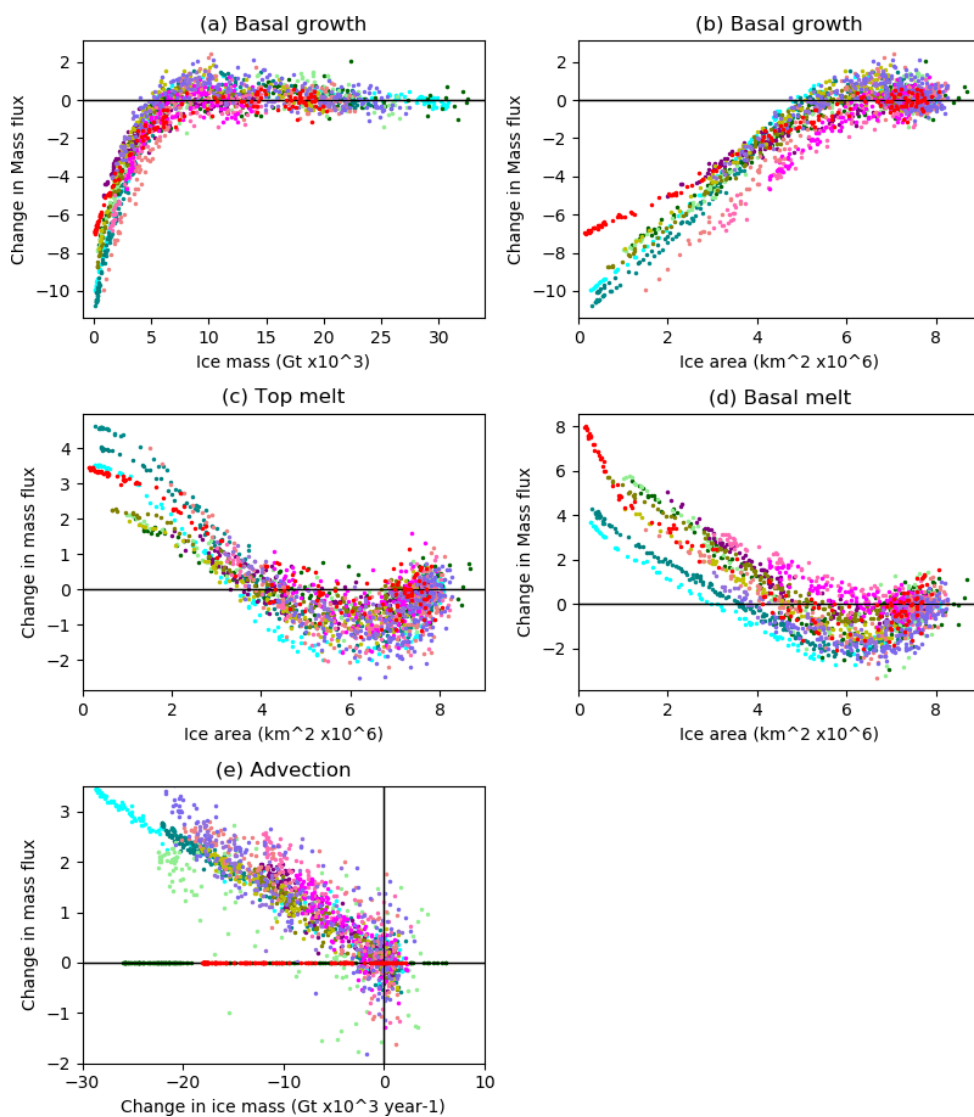
Figure 11: Selected annual mean components of the Arctic sea ice mass budget for all the models, plotted against ice state. All values are summed over the region shown in Fig. 1. The budget components are anomalies relative to the 1960-89 mean, with units of kg year^{-1} (a) Basal growth vs ice mass (b) Basal growth vs ice area (c) Top melt vs ice area (d) Basal melt vs ice area (e) Advection vs change in ice mass (relative to 1960-89).
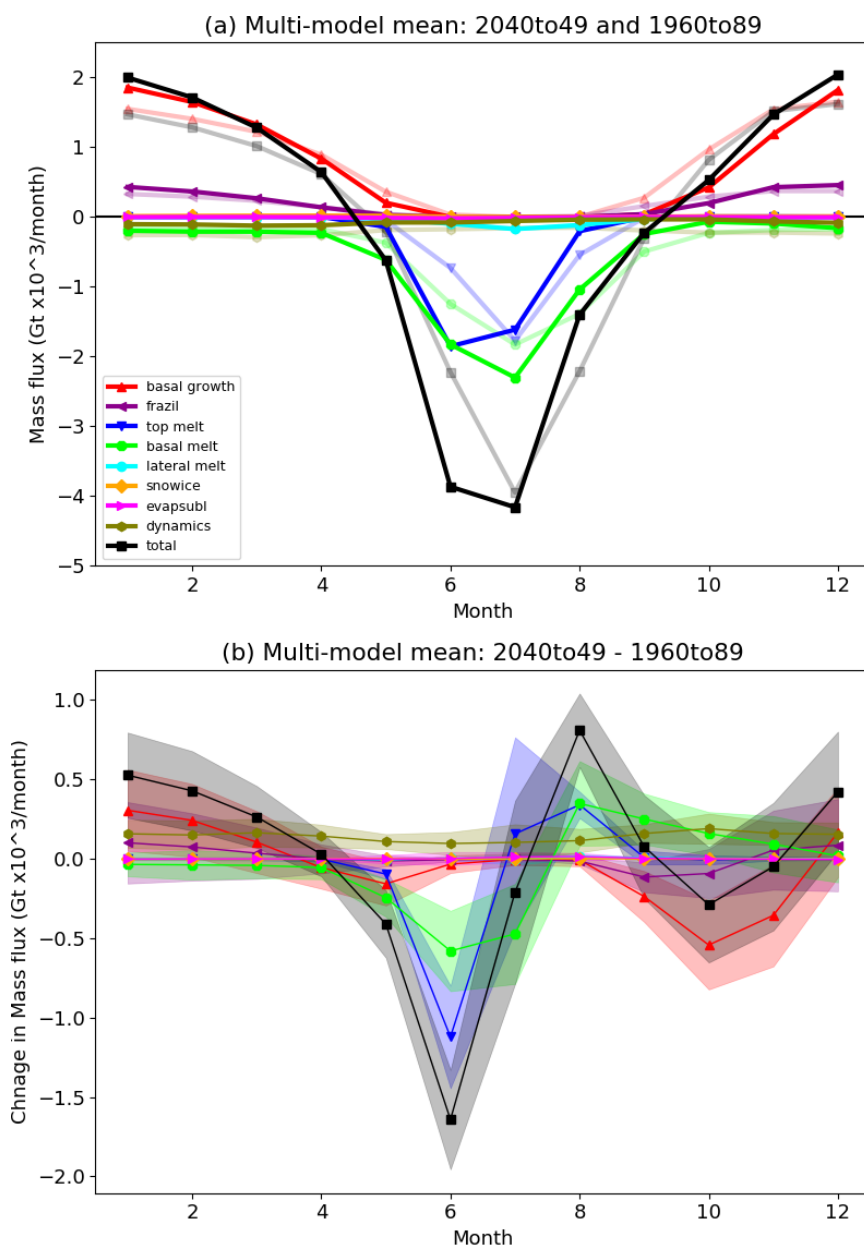
965

Figure 12: Seasonal cycles of components of the Arctic sea ice mass budget for the multi-model mean. Values are summed over the region shown in Fig. 1. For each budget component, the multi-model mean is calculated by averaging the ensemble means for each model with data for that component. (a) Cycles for 1960-89 (faint) and 2040-90 (bold) (b) Difference (2040-49 – 1960-89).

970
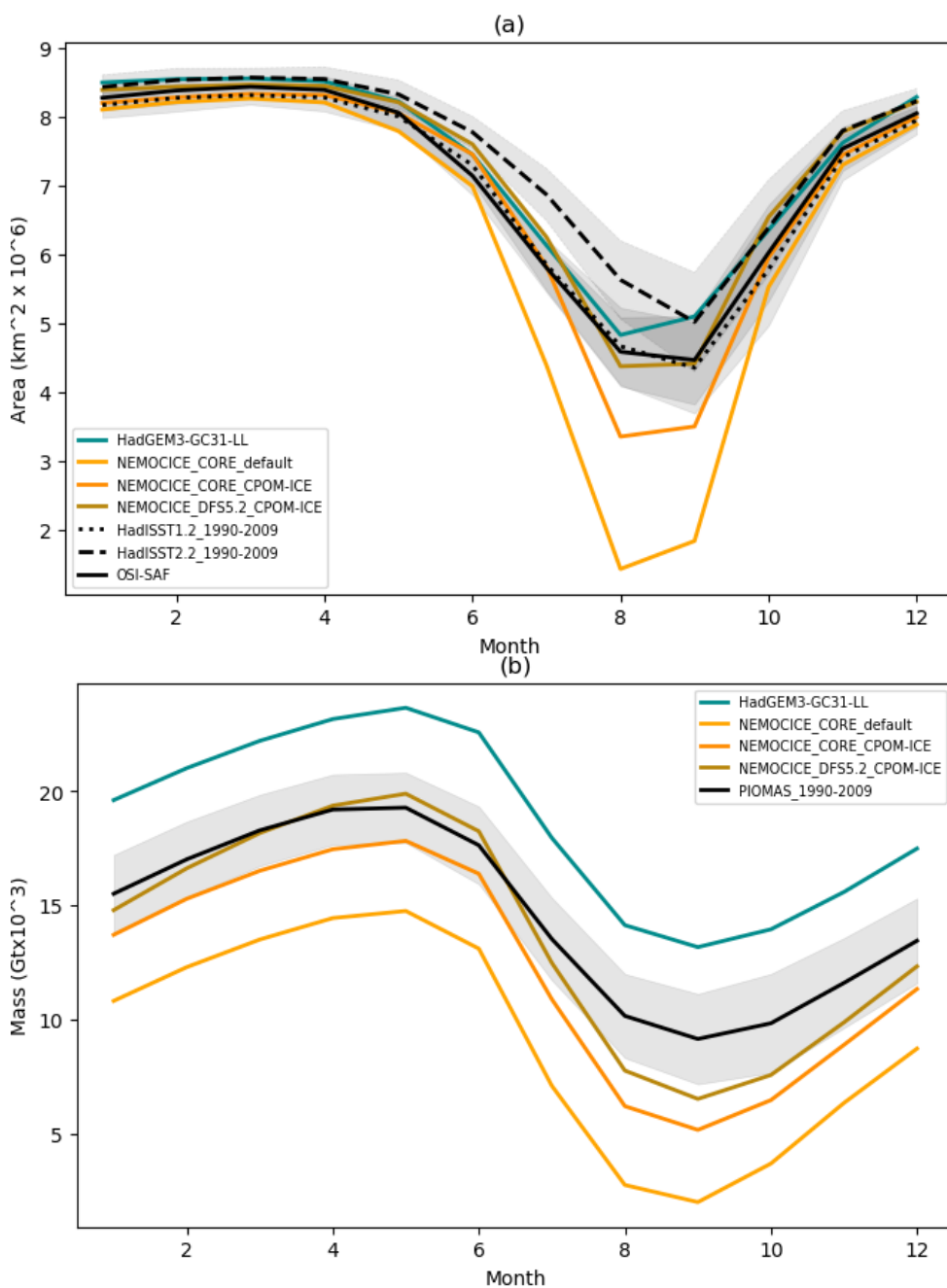
Figure 13: Seasonal cycles of (a) ice area and (b) ice volume for the reference period 1990-2009
975   *budget, for the forced ocean-ice runs (Table 3), plus HadGEM3-GC31-LL. Where more than one model*
integration is available, the values are ensemble means. Also shown is data for the same periods for
(a) the HadISST1.2 (Rayner et al., 2003), HadISST.2.2 (Titchner and Rayner, 2014), and OSI-SAF (OSI-
SAF, 2017) observational datasets, and (b) PIOMAS reanalysis (Zhang and Rothrock, 2003) for the
same period. The shaded regions show +/- 1 standard deviation in the monthly values.

980
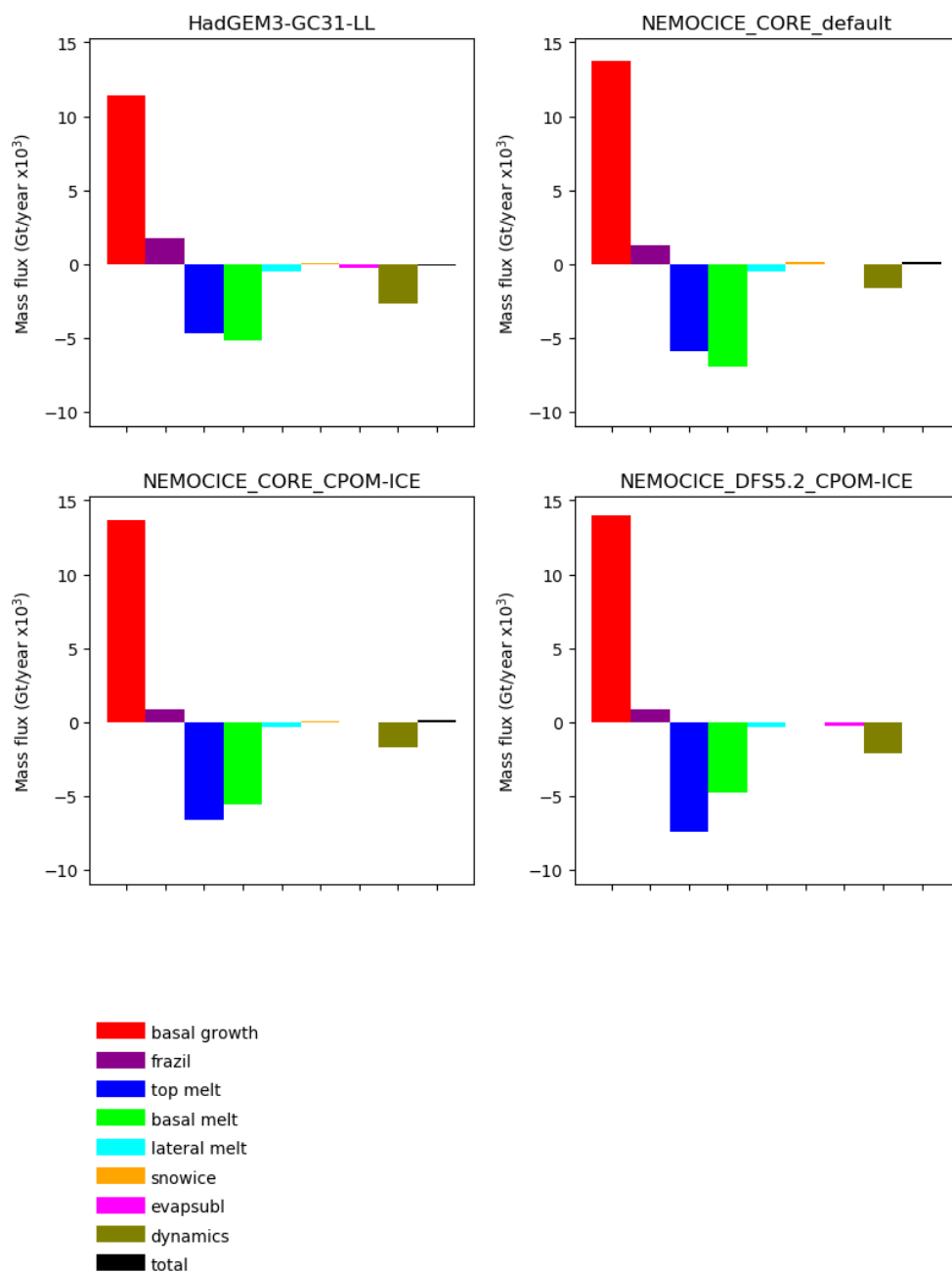
Figure 14: Components of the annual mean Arctic sea ice mass budget for the forced ocean-ice runs, plus HadGEM3-GC31-LL. Values are summed over the region shown in Fig. 1, for the period 1960-89.